Title

Three-dimensional variations in Love and Rayleigh wave azimuthal anisotropy for the upper 800 km of the mantle

Authors

Yuan, Kaiqing
Beghein, Caroline

Publication Date

2014-04-01

DOI

10.1002/2013jb010853

Peer reviewed

Three-dimensional variations in Love and Rayleigh wave azimuthal anisotropy for the upper 800 km of the mantle

Kaiqing Yuan[1] and Caroline Beghein[1]

[1]*Department of Earth, Planetary, and Space Sciences, University of California Los Angeles, Los Angeles, CA 90095, USA. E-mail: kqyuan@ucla.edu; cbeghein@ucla.edu*

Key Points:

- A new model of azimuthal anisotropy for horizontally polarized shear waves is presented
- 1% anisotropy is detected in the mantle transition zone
- Horizontally polarized shear wave anisotropy changes at the LAB and top of transition zone

ABSTRACT

We present a new mantle model (YB14SHani) of azimuthal anisotropy for horizontally polarized shear-waves (SH) in parallel with our previously published vertically polarized shear-wave (SV) anisotropy model (YB13SVani). YB14SHani was obtained from higher mode Love wave phase velocity maps with sensitivity to anisotropy down to ~1200 km depth. SH anisotropy is present down to the mantle transition zone (MTZ) with an average amplitude of ~2% in the upper 250 km and ~1% in the MTZ, consistent with YB13SVani. Changes in SV and SH anisotropy were found at the top of the MTZ where olivine transforms into wadsleyite, which might indicate that MTZ anisotropy is due to the lattice preferred orientation of anisotropic material. Beneath oceanic plates, SV fast axes become sub-parallel to the absolute plate motion (APM) at a depth that marks the location of a thermally controlled lithosphere-asthenosphere boundary (LAB). In contrast, SH anisotropy does not systematically depend on ocean age. Moreover, while upper mantle SV anisotropy is anomalously high in the middle of the Pacific, as seen in radial anisotropy models, SH anisotropy amplitude remains close to the average for other oceans. Based on the depth at which SV fast axes and the APM direction begin to align, we also found that the average thickness of cratonic roots is ~ 250 km, consistent with

29 *Yuan and Romanowicz* [2010] for North America. Here, we add new constraints on the
30 nature of the cratonic LAB and show that it is characterized by changes in both SV and
31 SH anisotropy.

32 **Key words:** Surface waves and free oscillations, Tomography, Mantle

33 **1. INTRODUCTION**

34 The presence of seismic anisotropy, which is the directional dependence of seismic wave
35 velocity, is required to explain a variety of seismic data. We often distinguish between
36 azimuthal and radial anisotropy (also called polarization anisotropy or transverse
37 isotropy). Azimuthal anisotropy characterizes wave velocity variations within the
38 horizontal plane. Radial anisotropy quantifies the change in wave velocity between the
39 horizontal and vertical directions of polarization or propagation. Evidence for radial
40 anisotropy in the uppermost mantle first came from the discrepancy between shear-wave
41 velocity models based on Rayleigh or Love wave dispersion data [*Anderson*, 1961].
42 Azimuthal anisotropy was first found beneath the Pacific from marine refraction
43 experiments [*Hess*, 1964]. Many studies have since then confirmed the presence of
44 seismic anisotropy in the top 250 km of the mantle and in the lowermost mantle (D"
45 layer).

46 The mechanism by which seismic anisotropy is generated is usually assumed to be either
47 shape preferred orientation (SPO) of isotropic structures with contrasting elastic
48 properties such as tubules or lenses, or lattice preferred orientation (LPO) of the
49 crystallographic axes of elastically anisotropic minerals. In the mantle lithosphere,
50 dislocation creep is likely to be the dominant deformation mechanism due to the presence

of high stress. Lithospheric "frozen-in" seismic anisotropy is generally attributed to olivine LPO relating to tectonic processes [*Karato*, 1989; *Nicolas and Christensen*, 2013; *Silver*, 1996] since this mineral has a high intrinsic anisotropy and aligns in the ambient stress field [*Ismaı□l and Mainprice*, 1998; *Karato*, 1989; *Nicolas and Christensen*, 2013; *Zhang and Karato*, 1995]. Asthenospheric anisotropy is often thought to be due to olivine LPO associated with present-day mantle deformation because the fast seismic direction often aligns with the absolute plate motion [*Becker et al.*, 2003; *Debayle et al.*, 2005; *Debayle and Ricard*, 2013; *Gung et al.*, 2003; *Smith et al.*, 2004; *Yuan and Romanowicz*, 2010; *Yuan and Beghein*, 2013], and the preferred alignment of olivine is often used to determine the direction of mantle flow [*Becker et al.*, 2003]. A recent experimental study reported, however, crystallographic preferred orientation (CPO) of iron-free olivine during diffusion creep [*Miyazaki et al.*, 2013]. This may alter common views of mantle deformation, but the authors demonstrated that even in the case of diffusion strong A-type fabric, i.e. with the fast axis almost parallel to the direction of mantle flow, is expected in the asthenosphere. In the D" layer, horizontal layering or aligned inclusions of a material with contrasting shear-wave properties was first proposed to explain observations of seismic anisotropy [*Kendall and Silver*, 1996]. More recent work has however shown that LPO of the post-perovskite phase offers another possible explanation [*Oganov et al.*, 2005].

While the top 250 km of the mantle and the D" layer are seismically anisotropic, the presence of seismic anisotropy in the deep upper mantle and bulk of the lower mantle is uncertain. There is, however, growing evidence for seismic anisotropy at greater depths than previously thought, both in shear-wave splitting measurements [*Foley and Long*,

74 2011; *Fouch and Fischer*, 1996; *Wookey et al.*, 2002] and in global tomographic models
75 [*Beghein and Trampert*, 2004; *Beghein et al.*, 2006; *Ferreira et al.*, 2010; *Kustowski et*
76 *al.*, 2008; *Montagner and Kennett*, 1996; *Panning and Romanowicz*, 2004; 2006;
77 *Trampert and van Heijst*, 2002; *Visser et al.*, 2008b; *Yuan and Beghein*, 2013].
78 Determining its presence inside and near the mantle transition zone (MTZ) is,
79 nevertheless, important to gain insight on the style of mantle convection, which directly
80 relates to the thermochemical evolution of the planet. Existing models of radial
81 anisotropy present large discrepancies, however, and they are unable to robustly constrain
82 whether the vertical or horizontal direction is faster for seismic wave propagation at those
83 depths [*Beghein and Trampert*, 2004; *Beghein et al.*, 2006; *Ferreira et al.*, 2010;
84 *Kustowski et al.*, 2008; *Montagner and Kennett*, 1996; *Panning and Romanowicz*, 2004;
85 2006; *Visser et al.*, 2008b]. Some of the differences between models are due to the
86 inherent non-uniqueness of the inverse problem [*Beghein et al.*, 2006; *Visser et al.*,
87 2008b], whereas others originate from the chosen prior crustal model [*Ferreira et al.*,
88 2010], the method employed to calculate crustal corrections [*Lekić and Panning*, 2010],
89 and prior assumptions regarding the anisotropic parameters [*Beghein and Trampert*,
90 2004; *Beghein et al.*, 2006]. In addition, the commonly proposed interpretation of radial
91 anisotropy models in terms of LPO has recently been challenged [*Wang et al.*, 2013] and
92 a combination of LPO and fine layering may have to be invoked at least in the upper
93 250km of the mantle. This would render the use of radial anisotropy models to constrain
94 mantle flow very difficult.

95 Until recently, very few models of azimuthal anisotropy displayed any significant signal
96 below 250 km depth. This was mostly due to the limited vertical resolution of the data

97 employed. However, *Trampert and van Heijst* [2002] and *Beghein et al.* [2008] showed
98 that long period surface wave overtones and Earth's free oscillation data, respectively, are
99 compatible with the presence of azimuthal anisotropy in the MTZ. More recently, we
100 modeled three-dimensional (3-D) global variations in vertically polarized shear-wave
101 azimuthal anisotropy from the inversion of Rayleigh wave higher modes [*Yuan and*
102 *Beghein*, 2013]. These data have sensitivity to mantle structure down to about 1400 km
103 depth and enabled us to determine that about 1% SV wave azimuthal anisotropy is
104 present between 300 km to 800 km depth. In addition, we showed that, on average, the
105 fast azimuth of propagation for SV waves changes across the mantle transition zone
106 boundaries where phase changes are believed to occur. Because of the correlation
107 between the location of phase transformations and changes in anisotropy amplitude and
108 fast axes direction, we suggested that the detected MTZ anisotropy is linked to the nature
109 and composition of the MTZ and caused by LPO of wadsleyite and ringwoodite.

110 The goal of the present paper is to extend our previous global study of SV azimuthal
111 anisotropy by adding constraints on horizontally polarized shear-wave azimuthal
112 anisotropy. In particular, we aim at determining whether SH anisotropy is present in the
113 deep upper mantle, and whether changes in anisotropy across the MTZ boundaries found
114 in SV waves [*Yuan and Beghein*, 2013] can also be detected for SH anisotropy. We thus
115 inverted anisotropic Love wave fundamental and higher mode phase velocity maps,
116 which are sensitive to SH anisotropy down to depths of about 1200 km. While
117 insufficient mineral physics data are currently available to uniquely interpret models of
118 SV anisotropy in the MTZ in terms of mantle deformation, adding constraints on another
119 elastic parameter will facilitate future interpretation of the results.

2. DATA

The data used in this study are the anisotropic phase velocity maps obtained by *Visser et al.* [2008a] for Love wave fundamental modes and the first five overtones at periods comprised between 35 s and 175 s. More specifically, there were 16 fundamental modes between 35 s and 175 s, 16 first overtones between 35 s and 175 s, 13 second overtones between 25 s and 115 s, 10 third overtones between 35 s and 79 s, eight fourth overtones between 35 s and 63 s, and seven fifth overtones between 35 s and 56 s. The dispersive properties of surface waves make them ideal to provide depth constraints on Earth's internal structure. While commonly used fundamental mode surface waves (periods between 50 s and 200 s) cannot resolve mantle structure beyond 250 km depth, the use of higher modes provide significantly improved sensitivity to larger depths. We were able to extend the sensitivity to the deep upper mantle and top of the lower mantle (Fig. 1).

Relative perturbations in surface wave phase velocity c in a slightly anisotropic medium can be expressed as [*Montagner and Nataf*, 1986]:

$$dc/c(T,\Psi) = c_0(T) + c_1(T)\cos 2\Psi + c_2(T)\sin 2\Psi + c_3(T)\cos 4\Psi + c_4(T)\sin 4\Psi \quad (1)$$

T is the period of the wave and Ψ is the azimuth of propagation. c_0 is the phase velocity anomaly averaged over all azimuths, and c_i $(i=1,...,4)$ are anisotropic terms that represent the azimuthal dependence of the phase velocity. The relative phase velocity perturbations are determined with respect to a spherically symmetric reference Earth model. *Yuan and Beghein* [2013] modeled 3-D variations in SV azimuthal anisotropy using the 2Ψ anisotropy terms (c_1 and c_2) of the Rayleigh wave phase velocity maps obtained by *Visser et al.* [2008a]. In the present study, we used the 4Ψ terms (c_3 and c_4) of *Visser et al.*

142 [2008a]'s Love wave phase velocity maps to build a 3-D model of SH azimuthal
143 anisotropy.

144 *Visser et al.* [2008a] found that anisotropy was required in the construction of the phase
145 velocity maps to explain their measurements for both Love and Rayleigh waves. They
146 showed that the two types of surface wave data required 2Ψ and 4Ψ terms, even for
147 fundamental modes. *Montagner and Tanimoto* [1991] demonstrated, however, that a 4Ψ-
148 dependence is not expected in fundamental mode Rayleigh waves for realistic
149 petrological models, and a 2Ψ-dependence is not expected for fundamental mode Love
150 waves. These petrological arguments are often used to help determine the strength of
151 anisotropy in fundamental mode phase velocity maps because it cannot be determined by
152 the data alone and has therefore to be fixed by other constraints. Rayleigh wave 4Ψ and
153 Love wave 2Ψ terms are thus generally strongly damped.

154 In the study of *Visser et al.* [2008a], however, the Rayleigh wave data fit was
155 significantly improved when including a 4Ψ-dependence. These 4Ψ terms could, in
156 theory, help constrain SH anisotropy, but the sensitivity of the fundamental and higher
157 modes to SH anisotropy is very small. Rayleigh wave phase velocity maps are better
158 suited to constrain SV anisotropy by inversion of the 2Ψ terms, and SH anisotropy is best
159 constrained by Love wave 4Ψ terms. Similarly, Love wave 2Ψ terms could potentially
160 offer additional constraints on SV anisotropy. However, as discussed by *Visser et al.*
161 [2008a], it is likely that the need for 2Ψ anisotropy in their fundamental Love wave phase
162 velocity maps was driven by Love-Rayleigh coupling, implying that Love waves cannot
163 be used reliably to invert for SV anisotropy. This was initially speculated by *Montagner*

164 *and Tanimoto* [1990] and later demonstrated by *Sieminski et al.* [2007]. While there is no
165 evidence *a priori* that such coupling is also responsible for the 2Ψ terms in the higher
166 mode Love wave phase velocity maps of *Visser et al.* [2008a], it cannot be ruled out yet.
167 We thus prefer to employ the Love wave higher mode data to constrain SH anisotropy
168 only, and to use Rayleigh waves to constrain SV anisotropy. Most importantly, *Visser et*
169 *al.* [2008a] established that the Love wave 4Ψ anisotropy terms did not depend on
170 whether 2Ψ terms were included in the construction of the phase velocity maps.

171 *Visser et al.* [2008a] were able to obtain dispersion measurements of higher modes for a
172 larger number of overtones than previously published by using a model space search
173 approach. Overtones are inherently difficult to separate, but the use of the Neighbourhood
174 Algorithm [*Sambridge*, 1999a; b] enabled them to determine the statistical significance of
175 their measurements for the different modes, i.e. they were able to determine the number
176 of higher modes reliably constrained by the seismograms. Their method also provided
177 consistent phase velocity uncertainties. The lateral resolution of their phase velocity maps
178 generally decreases with increasing overtone number. The authors estimated that
179 fundamental mode models are resolved up to spherical harmonic degree 8 for the 2Ψ
180 terms and spherical harmonic degree 9 for the 4Ψ terms. For the higher modes the lateral
181 resolution was estimated to be of degree 5 and degree 6 for the 2Ψ and 4Ψ maps,
182 respectively. This implies a resolving power of about 4500 km near the surface,
183 decreasing to ~6500 km near MTZ depths. This change in resolution with depth is due to
184 a reduction in the quality of the path azimuthal coverage resulting from a lower number
185 of modes measured reliably as the overtone number increases (see Fig. 2 of *Visser et al.*
186 [2008a]). This affected the ray coverage in the southeastern Pacific, southern Indian

187 Ocean, and southern Atlantic for the third through fifth higher modes. Ray coverage was
188 however very good everywhere for the fundamental modes, and in most continental
189 regions and the northwestern Pacific for the higher modes. Another factor that affected
190 the resolution of the maps is the choice of the damping made by the authors. Their choice
191 was such that the relative model uncertainty remained constant for all modes, resulting in
192 phase velocity maps of decreasing resolution with increasing overtone number. Because
193 the inferences made in this paper focus on large-scale anisotropy, using data of varying
194 resolution should not strongly affect our results.

195 Another common source of uncertainty when constructing anisotropic phase velocity
196 maps is the existence of trade-offs between the different terms of Eq. (1), which can
197 result in lateral heterogeneities or topography at discontinuities being mapped into the
198 anisotropy. The resolution matrices calculated by *Visser et al.* [2008a] showed that there
199 was little mapping of isotropic structure into the anisotropic terms. However, resolution
200 matrices are functions of the regularization and parameterization applied, and are not
201 ideal to evaluate the parameter trade-offs. In addition, despite the authors' best efforts to
202 minimize these trade-offs, one cannot completely separate the different terms because
203 data coverage is imperfect owing to the uneven distribution of earthquakes and seismic
204 stations over the globe. The phase velocity maps employed here consist, nevertheless, of
205 a unique dataset of anisotropic higher mode Love waves and, keeping the caveats listed
206 above in mind, our study should be seen as a first step toward mapping 3-D SH
207 anisotropy in the mantle.

208 **3. METHODS**

3.1. Parameterization and Inversion

We modeled 3-D variations in SH anisotropy by inverting the 4Ψ terms (c_3 and c_4) of Eq. (1) for Love wave fundamental and higher modes [*Montagner and Nataf*, 1986]. These anisotropic terms are depth integrals of perturbations in elastic parameters E_c and E_s that relate to SH azimuthal anisotropy:

$$c_3(T) = \int \frac{E_c(r)}{N(r)} K_E(r,T)dr \quad (2)$$

$$c_4(T) = \int \frac{E_s(r)}{N(r)} K_E(r,T)dr \quad (3)$$

$K_E(r,T)$ represents the local partial derivative, also called sensitivity kernel, for relative perturbations in E_c and E_s with respect to Love parameter N [*Love*, 1927] at period T and radius r. Love parameter N is the elastic parameter that determines the velocity of horizontally polarized shear-waves. These sensitivity kernels were calculated based on normal mode theory [*Takeuchi and Saito*, 1972]. SH azimuthal anisotropy amplitude E and fast propagation azimuth Θ are given by:

$$E = \sqrt{E_s^2 + E_c^2} \quad (4)$$

and

$$\Theta = \frac{1}{4}\arctan(E_s/E_c) \quad (5)$$

Although the crust does not seem to have a strong effect on one-dimensional (1-D) shear-wave velocity and anisotropy models [*Marone and Romanowicz*, 2007; *Yuan and Beghein*, 2013], it has been demonstrated that 3-D variations in crustal structure and their

effect on the partial derivatives can affect 3-D mantle models [*Boschi and Ekström*, 2002; *Bozdağ and Trampert*, 2010; *Kustowski et al.*, 2007; *Marone and Romanowicz*, 2007]. By performing accurate crustal corrections one can reduce the mapping of crustal structure into the deep mantle. In order to account for the effect of the crust on the partial derivatives, we thus adopted an approach similar to that of *Boschi and Ekström* [2002]. We parameterized the Earth's surface using $2° \times 2°$ cells following crustal model CRUST2.0 [*Bassin et al.*, 2000], and created a local reference Earth model composed of PREM [*Dziewonski and Anderson*, 1981] and CRUST2.0 at each grid cell. Sensitivity kernels were calculated based on the new local reference model (Fig. S1). Inversions of c_3 and c_4 were performed independently from one another at each grid cell using the local sensitivity kernels, and the anisotropy amplitude and fast directions were calculated on the grid using equations (4) and (5).

$E_s(r)$ and $E_c(r)$ were parameterized vertically using 18 cubic spline functions $S_i(r)$ of varying depth spacing between the surface and 1400 km (Fig. 2):

$$E_c(r) = \sum_{i=1}^{18} E_c^i S_i(r) \quad (6)$$

$$E_s(r) = \sum_{i=1}^{18} E_s^i S_i(r) \quad (7)$$

The inverse problem can be written as:

$$\mathbf{d} = \mathbf{A}\mathbf{m} \quad (8)$$

$\mathbf{d}$ is a vector containing the 4Ψ coefficient, $\mathbf{m}$ is a vector containing the model parameters, which are the spline coefficients E_c^i or E_s^i, and $\mathbf{A}$ is the matrix whose elements $\mathbf{A_{ij}}$ are the integral of the j-th sensitivity kernel $K_j(r)$ weighted by the i-th spline $S_i(r)$:

$$A_{ij} = \int K_j(r) S_i(r) dr \quad (9)$$

We solved Eq. (8) for E_c and E_s separately at each grid cell using a singular value decomposition method [*Jackson*, 1972; *Lanczos*, 1961; *Wiggins*, 1972] in which $\mathbf{A}$ is a $n \times m$ matrix decomposed into the product:

$$\mathbf{A} = \mathbf{U}\boldsymbol{\Lambda}\mathbf{V}^T \quad (10)$$

$\mathbf{U}$ is a $n \times n$ matrix of eigenvectors that span the data space, $\mathbf{V}$ is a $m \times m$ matrix of eigenvectors that span the model space, and $\boldsymbol{\Lambda}$ is a $n \times m$ diagonal matrix whose columns are nonnegative eigenvalues λ_i. It can be shown that $\mathbf{A}\mathbf{A}^T$ and $\mathbf{A}^T\mathbf{A}$ have the same p non-zero eigenvalues λ_i^2. These λ_i^2 are called the singular values of $\mathbf{A}$ and are often ranked by decreasing magnitude. $\boldsymbol{\Lambda}$ can be partitioned into a $p \times p$ submatrix $\boldsymbol{\Lambda}_p$ containing the p non-zero eigenvalues and a zero submatrix $\boldsymbol{\Lambda}_0$:

$$\lambda_i = \lambda_j \text{ if } i = j, i \leq p \quad (11)$$

$$\lambda_i = 0 \text{ if } i > p \ (i = 1, \dots, m) \quad (12)$$

$$\lambda_j = 0 \text{ if } j > p \ (j = 1, \dots, n) \quad (13)$$

We then have $\mathbf{U}\boldsymbol{\Lambda}\mathbf{V}^T = \mathbf{U}_p\boldsymbol{\Lambda}_p\boldsymbol{V}_p^T$ where $\mathbf{U_p}$ is a $n \times p$ matrix whose columns are the p eigenvectors $\mathbf{u}_i$ (i=1,...,p) of $\mathbf{A}\mathbf{A}^T$ that have non-zero eigenvalues. $\mathbf{V_p}$ is a $m \times p$ matrix whose columns are the p eigenvectors $\mathbf{v}_i$ of $\mathbf{A}^T\mathbf{A}$ that have non-zero eigenvalues.

The generalized inverse of $\mathbf{A}$ can then be written as:

$$\mathbf{A}^{-1} = \mathbf{V}_p\boldsymbol{\Lambda}_p^{-1}\mathbf{U}_p^T \quad (14)$$

and the estimated model parameters $\mathbf{m}^{\mathrm{est}}$ are given by:

$$\mathbf{m}^{\mathrm{est}} = \mathbf{V}_{\mathrm{p}}\boldsymbol{\Lambda}_{\mathrm{p}}^{-1}\mathbf{U}_{\mathrm{p}}^{\mathrm{T}}\mathbf{d} \quad (15)$$

The sum in Eq. (15) is thus limited to the non-zero eigenvalues only, thereby reducing instabilities in the solution that can be caused by null eigenvalues.

Because the smallest non-zero eigenvalues can also generate instabilities in the inverse problem, care needs to be exercised in choosing the number of eigenvalues that will contribute to the solution. *Wiggins* [1972] proposed to construct the inverse operator from the $q \leq p$ largest eigenvalues and corresponding eigenvectors. Here, we followed *Matsu'Ura and Hirata* [1982] to determine the cutoff number of eigenvalues. Their approach consists in normalizing matrix $\mathbf{A}$ by the data covariance matrix $\mathbf{C_d}$ and the prior model covariance matrix $\mathbf{C_m}$:

$$\mathbf{A}^{\dagger} = \mathbf{C}_{\mathrm{d}}^{-1}\mathbf{A}\mathbf{C}_{m} \quad (16)$$

$\mathbf{A}^{\dagger}$ is the normalized matrix, and to keep all eigenvalues that are smaller or equal to unity: the sum is over all $\lambda_{\mathrm{i}} \geq 1$. We employed the uncertainties estimated by *Visser et al.* [2008a] for their phase velocity maps to build the data covariance matrix. With the employed method, the regularization is implicit in the choice of the prior model covariance matrix and modifying $\mathbf{C_m}$ is equivalent to changing the regularization in a least square inversion [*Snieder and Trampert*, 2000] as it yields a different cutoff in the number of eigenvalues. The model resolution matrix $\mathbf{R}$ reflects how well the true model, $\mathbf{m}^{\mathrm{true}}$, was represented by the estimated model, $\mathbf{m}^{\mathrm{est}}$, and the trade-offs among the model parameters:

$$\mathbf{m}^{\text{est}} = \mathbf{R}\mathbf{m}^{\text{true}} \quad (17)$$

If $\mathbf{R}=\mathbf{I}$, then $\mathbf{m}^{\text{est}}= \mathbf{m}^{\text{true}}$ and the parameters are perfectly resolved. Calculating a resolution matrix can be computationally prohibitive for large inverse problems. Here, however, because we solved Eq. (8) for E_c and E_s separately at each grid cell, thereby dividing the inverse problem into $2N_c$ small size inverse problems (of 18 unknowns each), where N_c is the number of grid cells, we were able to calculate the resolution matrix by singular value decomposition. The resolution matrix $\mathbf{R}$ is then given by [*Menke*, 1989]:

$$\mathbf{R} = (\mathbf{A}^{\dagger})^{-g}\mathbf{A}^{\dagger} = (\mathbf{V}_p\mathbf{\Lambda}_p^{-1}\mathbf{U}_p^{T})(\mathbf{U}_p\mathbf{\Lambda}_p\mathbf{V}_p^{T}) = \mathbf{V}_p\mathbf{V}_p^{T} \quad (18)$$

3.2 Generalized Spherical Harmonics, Power Spectrum, and Correlation

In order to calculate the power spectra of our SH anisotropy model and that of *Yuan and Beghein* [2013]'s SV anisotropy model, we expanded the models in generalized spherical harmonics [*Phinney and Burridge*, 1973; *Trampert and Woodhouse*, 2003] up to degree 20 and calculated the power spectrum for each anisotropic parameter following *Becker et al.* [2007]. The azimuthal dependence of the phase velocity described by Eq. (1) can be rewritten using tensors rather than scalars [*Trampert and Woodhouse*, 2003]:

$$dc/c(\omega, \Psi) = c_0(\omega) + \tau_{ij}\nu_i\nu_j + \sigma_{ijkl}\nu_i\nu_j\nu_k\nu_l \quad (19)$$

Indices i,j,k,l take values of 1 and 2 corresponding to the latitude and the longitude, respectively. $\boldsymbol{\nu} = (-\cos\Psi, \sin\Psi)$ is a unit vector in the direction of propagation. $\boldsymbol{\tau}$ and $\boldsymbol{\sigma}$ are symmetric and trace-free tensors on the 2-D spherical surface. Their two independent components are given by:

$$\tau_{\theta\theta} = \tau_{\phi\phi} = c_1(\omega) \quad (20)$$

$$\tau_{\theta\phi} = \tau_{\phi\theta} = -c_2(\omega) \quad (21)$$

$$\sigma_{\theta\theta\theta\theta} = \sigma_{\theta\theta\phi\phi} = -\sigma_{\phi\phi\phi\phi} = c_3(\omega) \quad (22)$$

$$\sigma_{\theta\theta\theta\phi} = -\sigma_{\phi\phi\phi\theta} = -c_4(\omega) \quad (23)$$

The non-zero contravariant components of these tensors are given by:

$$\tau^{++} = c_1(\omega) + ic_2(\omega) \quad (24)$$

$$\tau^{--} = c_1(\omega) - ic_2(\omega) \quad (25)$$

$$\sigma^{++++} = c_3(\omega) + ic_4(\omega) \quad (26)$$

$$\sigma^{----} = c_3(\omega) - ic_4(\omega) \quad (27)$$

τ^{++} and τ^{--} are thus complex conjugate of each other, and so are $\sigma^{++++}$and σ^{----}.

Phinney and Burridge [1973] showed that the contravariant components of a tensor $\mathbf{M}$ of any rank can be expanded in generalized spherical harmonics:

$$m^{\alpha\beta\delta\cdots}(\theta,\phi) = \sum_{l=\alpha+\beta+\delta+\cdots}^{\infty} \sum_{m=-l}^{l} M_l^{\alpha\beta\delta\cdots} Y_l^{Nm}(\theta,\phi) \quad (28)$$

The first sum starts at $l = 2$ for a second order tensor and at $l = 4$ for a fourth order tensor. The 2Ψ and 4Ψ anisotropy can thus be expanded as:

$$\tau^{++}(\theta,\phi) = \sum_{l=2}^{L} \sum_{m=-l}^{m=l} \tau_{lm}^{++} Y_l^{2m}(\theta,\phi) \quad (29)$$

$$\tau^{--}(\theta,\phi) = \sum_{l=2}^{L} \sum_{m=-l}^{m=l} \tau_{lm}^{--} Y_l^{2m}(\theta,\phi) \quad (30)$$

$$\sigma^{++++}(\theta,\phi) = \sum_{l=4}^{L} \sum_{m=-l}^{m=l} \sigma_{lm}^{++++} Y_l^{4m}(\theta,\phi) \quad (31)$$

$$\sigma^{----}(\theta,\phi) = \sum_{l=4}^{L}\sum_{m=-l}^{m=l}\sigma_{lm}^{----}Y_l^{4m}(\theta,\phi) \quad (32)$$

For a generalized spherical harmonic expansion up to degree L the number of coefficients for the 2Ψ terms is $N^{2\psi} = (2L+6)(L-1)$ because $Y_l^{2m} = 0$ for $l < 2$, and the number of coefficients for the 4Ψ terms is $N^{4\Psi} = (2L+10)(L-3)$ because $Y_l^{4m} = 0$ for $l < 4$ [*Phinney and Burridge*, 1973; *Trampert and Woodhouse*, 2003].

Following and generalizing the definitions introduced by *Becker et al.* [2007], we define the spectral power at spherical harmonic degree l of the model as:

$$S_l = \sqrt{\frac{1}{N_l}\sum_{i=1}^{N_l} p_i^2} \quad (33)$$

N_l represents is the number of generalized spherical harmonic coefficients at degree l ($N_l = (2l+6)(l-1)$ for 2Ψ and $N_l = (2l+10)(l-3)$ for 4Ψ). p_i □s the i-th component of a vector containing the real and imaginary parts of the generalized spherical harmonic coefficients τ_{lm}^{++} or σ_{lm}^{++++} [*Boschi and Woodhouse*, 2006], depending on whether we calculate the spectra of the 2Ψ or 4Ψ model. We also adopt the same definition as *Becker et al.* [2007] for the correlation coefficient at degree l between two harmonic fields $\mathbf{q}$ and $\mathbf{p}$:

$$r_l = \frac{\sum_{i=1}^{N_l} p_i q_i}{\sqrt{\sum_{i=1}^{N_l} p_i^2}\sqrt{\sum_{i=1}^{N_l} q_i^2}} \quad (34)$$

To calculate a correlation between two models expanded up to degree L, one replaces N_l by the total number of coefficients used, i.e. $N^{2\Psi}$ for a 2Ψ model or $N^{4\Psi}$ for a 4Ψ model.

345 This expression is also valid for an azimuthally averaged model (0 term of Eq. (1)), in
346 which case the number of coefficients is $N^{0\Psi} = (L + 1)^2$.

347 **4. MODEL RESOLUTION AND ROBUSTNESS**

348 We performed several tests, described below, to assess the quality of our SH anisotropy
349 model. First, we tested that our main results, i.e. the presence of about 1% anisotropy in
350 the MTZ and amplitude minimum near the top of the MTZ as described in section 5, is
351 robust with respect to regularization. Second, we examined the vertical resolution of the
352 sensitivity kernels used in this study with a series of synthetic tests. The input models in
353 Fig. 3 simulate layering of SH anisotropy of decreasing amplitude with depth. We
354 obtained the output models by using the same data uncertainties as in the real data
355 inversions, and the same level of regularization as that chosen for our "preferred" model.
356 We tested inversions of synthetic data with and without added noise. The curves labeled
357 as "low noise" were obtained by perturbing each data by a random amount uniformly
358 drawn between −50% and +50% of its original value; for the curve labeled as "high
359 noise", relative perturbations were between −100% and +100%. These tests show that our
360 sensitivity kernels can resolve anisotropy amplitude in 80 km thick layers in the top 500
361 km of the mantle, 100 km thick layers in the top 600 km, and 120 km thick layers in the
362 upper 700 km. This is independent of the amount of noise added to the synthetic data.
363 The fast axes are not as well recovered as the amplitudes with added noise, but this is
364 mostly the case for a high level of noise and the corresponding recovered amplitudes are
365 often small. Other synthetic tests demonstrated that our inversion does not yield any
366 significant downward leakage even with added noise (Fig. S2). We have thus great depth
367 sensitivity throughout the upper mantle and MTZ.

368 Third, we calculated the resolution matrix for elastic parameter E_c (or identically for E_s)
369 obtained with our chosen regularization. Fig. 4 shows that the first 13 spline coefficients
370 (which correspond approximately to the top 800 km) are relatively well resolved with
371 little trade-offs among the different coefficients. The strongest trade-offs are found
372 between spline coefficients 3 through 5, which roughly correspond to depths between 100
373 km and 200 km (see Fig. 2).

374 Of course, the reader should be cautioned that the true resolution of the model is not
375 determined by the sensitivity kernels alone, but also by the lateral resolution of the phase
376 velocity maps as discussed in section 2. In addition, a resolution matrix, which depends
377 on the regularization applied, is not a perfect estimate of true parameter trade-offs. A
378 better approach to assess the robustness of our model would be to perform synthetic tests
379 with a 3-D input model of velocities and SH and SV anisotropy, which would be used to
380 predict and then invert phase velocity maps, seismograms, and along-path phase velocity
381 measurements. It would allow us to better explore the trade-offs between the isotropic
382 and anisotropic terms of the phase velocity map, but it is, unfortunately, computationally
383 very expensive and impractical. An even better approach would have been to explore the
384 model space and randomly sample 3-D velocity and anisotropy models to obtain statistics
385 on the best fitting models. Randomly generated models would be used to calculate along-
386 path phase velocities or full seismograms, which in turn would be compared to real data.
387 Such forward modeling methods have been applied to solve much smaller size problems
388 in the past (e.g. *Beghein* [2010]) and are better at quantifying model uncertainties and
389 parameter trade-offs. It would, however, be too time consuming and computationally
390 intensive to be feasible in the present case.

391 Finally, we performed statistical tests to determine whether the data used here require
392 deep SH anisotropy or whether a model with shallower anisotropy would be able to
393 explain the data equivalently well. Indeed, by allowing our inversion to extend to depths
394 of 1400 km, we found that our preferred best fitting model, displayed anisotropy in the
395 MTZ (see section 5). While a model with shallower anisotropy would likely not fit the
396 data as well, the presence of deep anisotropy might not be warranted by the data if the
397 misfit difference between the models results from an increase in the number of free
398 parameters rather than from the data themselves. To determine whether the data
399 employed truly require the presence of azimuthal anisotropy in the deep upper mantle, we
400 thus performed new inversions of the same dataset in which we require the anisotropy to
401 remain in the top 410 km (model A) and 670 km (model B). We then conducted F-tests
402 [*Bevington and Robinson*, 2002] to compare the misfit of YB14SHani to these new
403 models. F-tests are statistical tests that determine to what level of confidence the
404 difference in variance reduction is significant, and enable us to calculate the probability
405 that two models are equivalent. It makes use of the reduced χ^2 misfit defined in Eq. (35),
406 the number of independent parameters given by the trace M of the resolution matrix, and
407 the number N of data employed. The reduced χ^2 is given by *Trampert and Woodhouse*
408 [2003]:

409 $$\chi^2 = \frac{1}{\mathrm{N}-\mathrm{M}}(\mathbf{d}-\mathbf{Am})^{\mathrm{T}}\mathbf{C}_{\mathrm{d}}^{-1}(\mathbf{d}-\mathbf{Am}) \qquad (35)$$

410 where $\mathbf{d}$ is the data vector, $\mathbf{m}$ represents the model parameters, $\mathbf{A}$ is the kernel matrix, and
411 $\mathbf{C}_{\mathrm{d}}$ is the data covariance matrix. The reduced χ^2 and the trace of resolution matrix were

412 calculated at each grid cell for E_c and E_s separately in the three models. We then
413 calculated an average χ^2 following *Yuan and Beghein* [2013]:

414 $$\chi^2 = \frac{1}{2N_c}\sum_{i=1}^{N_c}(\chi_{s,i}^2 + \chi_{c,i}^2) \quad (36)$$

415 where N_c is the number of grid cells, and $\chi_{s,i}^2$ and $\chi_{c,i}^2$ are the reduced χ^2 for E_c and E_s at
416 grid cell i, respectively. F-tests were performed using these averaged misfits and showed
417 that the probability that model YB14SHani and model A are equivalent is less than 1%
418 (Fig. 5). Similarly, we calculated a 91.5% probability that YB14SHani is not equivalent
419 to model B.

420 **5. RESULTS AND DISCUSSION**

421 **5.1 Average Anisotropy**

422 In Fig. 6(a) and (c) we compare the root mean square (rms) amplitude of YB14SHani and
423 YB13SVani, and in Fig. 6(b) and (d) we display the global vertical auto-correlation
424 function of the 2Ψ and 4Ψ models, respectively. When analyzing azimuthal anisotropy
425 models, it is very useful to determine at which depth the fast axes for wave propagation
426 change direction significantly as this can indicate layering in the mantle [*Beghein et al.*,
427 2014; *Yuan and Romanowicz*, 2010; *Yuan and Beghein*, 2013]. In *Yuan and Beghein*
428 [2013] and *Beghein et al.* [2014] we calculated the vertical gradient of the SV fast axes
429 direction as a function of depth to locate where the strongest changes in anisotropy
430 occurred. It is, however, more difficult to quantify changes in fast axes direction with
431 depth for SH waves because of the 90° periodicity of the 4Ψ terms (Eq. (1)). Instead, we
432 calculated the vertical global auto-correlation (Eq. (32)) for the 4Ψ and 2Ψ models,

433 which we use as a proxy for the vertical gradient of the fast axes. The vertical auto-
434 correlation curves show how the anisotropy at one depth correlates with the anisotropy at
435 another depth. Here, we calculated this function using Eq. (34) and a 40 km widow
436 (correlation at depth z is the correlation between model at depth $z - 20$ km and model at
437 depth $z + 20$ km), and the model amplitudes were normalized so that the calculated
438 correlation reflects changes in fast axes only and does not account for vertical amplitude
439 changes. Comparison of Fig. 6(d) and Fig. 2(b) of *Yuan and Beghein* [2013] shows that
440 the depths at which the vertical auto-correlation is low for the 2Ψ model coincide with
441 depths at which the SV fast axes change direction significantly (i.e. where the vertical
442 gradients are high). We thus took a similar approach for the 4Ψ maps and chose to
443 associate low auto-correlation values for the 4Ψ model with changes in SH fast axes.

444 We found that the rms amplitude we obtained for G/L and E/N present several peaks in
445 the uppermost mantle (Fig. 6). It is the strongest in the top 200 km with a peak of 1.5-2%
446 for SH at 150 km depth and 2% for SV at 100 km depth, and both models display a
447 smaller peak around 50 km and 250 km depth. The G/L and E/N amplitudes are thus
448 consistent with one another and in agreement with previous estimates of SV anisotropy
449 amplitudes in global and regional models [*Debayle et al.*, 2005; *Yuan and Romanowicz*,
450 2010], with the exception of the new model of *Debayle and Ricard* [2013], which
451 displays amplitudes of ~3%. A recent study pointed out a large discrepancy between the
452 amplitude of upper mantle radial anisotropy (which can be as high as 8% on average) and
453 SV azimuthal anisotropy (typically of the order of 1-2% in the upper 200 km) in
454 tomographic models [*Wang et al.*, 2013]. The authors argued that LPO alone cannot
455 explain these differences and that we need to invoke an additional mechanism such as a

456 layered structure to reconcile the two types of observations. While our model amplitudes
457 appear to confirm that azimuthal anisotropy amplitudes are much lower than those of
458 radial anisotropy, for both SH and SV waves, caution needs to be taken before
459 interpreting such differences. Anisotropy amplitudes are strongly dependent on the
460 regularization applied during the construction of the phase velocity maps, and
461 regularization tends to lower amplitudes where spatial coverage is sparse or if the noise in
462 the data is high [*Chevrot and Monteiller*, 2009].

463 We also found that the SH and SV anisotropy amplitude minima are associated with
464 changes in fast axes for both SH and SV waves. This can be seen between 50 km and 100
465 km and at ~230 km depth, which is where the SV fast direction becomes sub-parallel to
466 the present-day absolute plate motion (APM) as shown by *Yuan and Beghein* [2013].
467 Most interestingly, the two parameters display ~1% anisotropy inside the MTZ and an
468 amplitude minimum at the top of the MTZ where the fast axes change direction. *Yuan*
469 *and Beghein* [2013] demonstrated that the changes in SV anisotropy between 50 km and
470 100 km depth and at ~230 km are not due to the chosen parameterization or the presence
471 of discontinuities at 80 km and 220 km depth in the reference model used to calculate the
472 sensitivity kernels. Similar tests were performed here for the SH model. We showed that
473 the minimum in dlnE between 50 km and 100 km depth is not the result of the chosen
474 depth parameterization by testing different parameterizations with more closely spaced
475 and less closely space spline functions (Fig. S3(a)). We also tested the effect of
476 discontinuities at 80 km and 220 km depth on the global average rms amplitude and
477 found no significant change in the model (Fig. S3(b)). Using the PREM crust instead of
478 CRUST2.0 resulted in some changes in the average amplitude profile in the top 200 km,

479 and shifted the amplitude minimum detected between 50 km and 100 km depth (Fig.
480 S3(b)), implying that crustal structure is important to resolve and interpret details in the
481 top 200 km of the model.

482 As discussed by *Yuan and Beghein* [2013] for SV anisotropy, the presence of 1% SH and
483 SV azimuthal anisotropy inside the MTZ could be due to the shape preferred orientation
484 of tilted layers of material with contrasting elastic properties. However, because we also
485 found changes in anisotropy near 410 km depth, where olivine is thought to go through a
486 phase transformation, we suggest that the origin of the observed seismic anisotropy is
487 more likely to be related to the nature of the MTZ. The detected amplitudes in the upper
488 MTZ are consistent with mineral physics estimates for wadsleyite anisotropy [*Kawazoe*
489 *et al.*, 2013; *Tommasi et al.*, 2004; *Zha et al.*, 1997], and the changes in fast axes at 410
490 km depth could simply be due to recrystallization during the phase change from olivine to
491 wadsleyite. The interpretation of these anisotropy changes in terms of mantle flow and
492 thermochemical evolution of the Earth is however not straightforward owing to the lack
493 of mineral physics data on MTZ material anisotropy. For instance, recrystallization of the
494 olivine structure during phase changes likely erases anisotropy before building up again,
495 and therefore could explain the changes in SH and SV anisotropy at 410km. The presence
496 of water inside or atop the transition zone might also change the anisotropic properties of
497 the olivine structure in the MTZ and how it relates to mantle flow direction, as it does at
498 uppermost mantle conditions [*Jung and Karato*, 2001]. Further investigations of the
499 effect of water, pressure, or partial melt on the anisotropy of ringwoodite and wadsleyite
500 are therefore needed before one can uniquely interpret our results.

501 **5.2 Global three-dimensional Model**

Figs. 7 and 8 display maps between 100 km and 600 km depth for models YB14SHani and YB13SVani, respectively. Large lateral variations in amplitude and fast axes are observed in both models, which might suggest a complex mantle flow pattern at depth. Interestingly, regions of high (or low) SV anisotropy do not necessarily coincide with high (or low) SH anisotropy. On the contrary, it even appears that in some areas the two types of anisotropy are anti-correlated. For instance, most of the high SV anisotropy area at 100 km depth in northeastern and central Pacific has low SH anisotropy and vice versa for the northwestern Pacific. Similar observations can be made at other depths: A high amplitude dlnE signal can be found in central Pacific in the MTZ, but dlnG is small in that region ($dlnG = G/L$ where L and G are elastic parameters that determine SV velocities and azimuthal anisotropy, respectively). This apparent anti-correlation between dlnG and dlnE is, nevertheless, not global (Fig. S4).

To our knowledge, the only other global inversion of 4Ψ anisotropy published so far is that of *Trampert and van Heijst* [2002] who used a slightly older higher mode Love wave dataset than in the present study. Because their study was focused on the MTZ, we can compare the models only at these depths. While there is general agreement between the models in terms of anisotropy amplitude in the MTZ, we found strong differences in the pattern of SH anisotropy. In both models, strong MTZ anisotropy can be found beneath Africa and the central Pacific, and low anisotropy near the East Pacific Rise, but the fast axes directions differ substantially. These discrepancies could result from differences in the datasets employed since they used the first and second overtone Love waves only, while the dataset we used here [*Visser et al.*, 2008a] contained Love wave fundamental and higher modes up to the fifth overtone. Discrepancies between the models could also

arise from the different inversion techniques employed. We performed a classical linear inversion in which one typically has to compromise between data fit and model size [*Snieder and Trampert*, 2000], whereas *Trampert and van Heijst* [2002] chose a *Backus and Gilbert* [1968] approach in which the resolution kernel is optimized towards a desired shape and depth range.

5.3 Anisotropy Beneath Oceanic Plates

Fig. 9 illustrates how SH and SV anisotropy vary beneath oceanic plates. A detailed discussion of YB13SVani under oceanic plates can be found in another paper [*Beghein et al.*, 2014]. Here we can compare YB13SVani with our new SH anisotropy model. Interestingly, we detect a change in uppermost mantle dlnE and dlnG with plate age only beneath the Pacific plate (Fig. 9(d) and (e)). In particular, the youngest parts of the Pacific plate present less SH anisotropy in the top 200 km than older regions (Fig. 9(g)), and less SV anisotropy than beneath the middle of the plate (Fig. 9(h)). We also find, as did *Nishimura and Forsyth* [1989], that uppermost mantle SV anisotropy amplitudes in the Pacific are the lowest for ages > 120 Ma (Fig. 9(h)). Remarkably, while SH amplitudes beneath the Pacific for mid-ages are close to the average values for other oceans (~2%), SV anisotropy is anomalously strong (up to 4%) in the 100-200 km depth range and for ages between ~40 Ma to ~120 Ma. Such a strong SV anisotropy is not found beneath other oceanic plates, though those are generally smaller than the Pacific plate and our data may not be able to resolve age differences beneath small plates.

We also note, as in *Yuan and Beghein* [2013] and *Beghein et al.* [2014], that the Pacific is characterized by an age dependence of the alignment of the SV fast axis with the APM

547 calculated using the no-net rotation reference model NNR-NUVEL 1A [*Gripp and*
548 *Gordon*, 2002]. Note that *Yuan and Beghein* [2013] demonstrated that using different
549 reference frames did not significantly change the results for the Pacific plate. We showed
550 [*Beghein et al.*, 2014] that the interface marking the change in SV fast axis direction,
551 from poor alignment with the APM at shallow depths to good alignment at greater depths
552 follows an isotherm with a mantle temperature of $900℃ - 1100℃$ in a half-space
553 cooling model [*Parker and Oldenburg*, 1973]. A similar observation can be made for
554 other oceans (Fig. 9): The fast SV wave direction tends to follow the APM over a
555 narrower depth range for older plates than for young ones. More specifically, the
556 alignment is good between ~150 km and 250 km depth for ages > 120 Ma and between
557 ~50 km and 250 km for ages lower than 80 Ma. In contrast, while SH anisotropy is lower
558 beneath young Pacific crust than older crust, it does not present any systematic age-
559 dependence, and the relative dlnE amplitude does not follow a half-space cooling model
560 (Figs. 9(g) and 10).

561 The reduction in SV anisotropy amplitude in the Pacific for ages > 120 Ma and between
562 100 km and 200 km was first detected by *Nishimura and Forsyth* [1989]. The authors
563 postulated that it relates to changes in the horizontal direction of anisotropic fabric with
564 depth rather than being due to a decrease of in situ anisotropy. They argued that the
565 significant differences in the direction of APM and fossil seafloor spreading in the
566 western Pacific might yield destructive interference of the shallow and deeper anisotropy
567 contributions. Here, we demonstrate that the lower SV anisotropy amplitude in the
568 western Pacific is close to the average amplitudes of other oceanic plates and is therefore
569 not anomalously low.

570 On the contrary, SV azimuthal anisotropy in the middle of the plate is anomalously high.
571 A similarly anomalous signal has also been observed in radial anisotropy models
572 [*Ekström and Dziewonski*, 1998; *Nettles and Dziewonski*, 2008; *Panning and*
573 *Romanowicz*, 2006], but its origin is not well understood. It appears, however, to coincide
574 with a layer of low shear-wave velocities in which the SV fast axes are subparallel to the
575 APM (see *Debayle and Ricard* [2013] and Fig. 9(i)). This anomalously high radial and
576 SV azimuthal anisotropies may result from deformation by dislocation creep in an
577 asthenospheric flow channel as previously suggested [*Gaboret et al.*, 2003; *Gung et al.*,
578 2003] or from CPO during diffusion creep [*Miyazaki et al.*, 2013]. Here, we show that,
579 interestingly, the Pacific plate asthenosphere does not display any anomalous SH
580 anisotropy, which may provide additional constraints on the origin of the signal in future
581 research.

582 No strong age dependence is found for SV anisotropy beneath ~200-250 km depth, but
583 changes in E/N are visible in the MTZ and at ~300 km depth: the anisotropy strength at
584 these depths is greater beneath oceans older than ~80Ma than under younger plates. We
585 verified that this is independent of the regularization applied (Fig. S5). In addition, we
586 think it is unlikely that these lateral variations result from vertical smearing or parameter
587 trade-offs (see section 4), although a full model space search will be needed in future
588 work to quantitatively assess these possibilities.

589 Interestingly, the map of SH anisotropy at 500 km depth (Fig. 7) reveals that this
590 apparent age signal comes primarily from the central Pacific and is oriented in the North-
591 South direction. While they are interesting, these variations may not have any physical
592 relation to crustal ages and could illustrate the complexity of the SH anisotropy signal at

593 these depths, possibly in relation to the geometry of the convective cells or to the Pacific
594 "superplume". However, we caution and remind the reader of the limited lateral
595 resolution of the data at these depths and the possibility that trade-offs between the
596 isotropic and anisotropic terms of the phase velocity maps may affect the strength of the
597 higher mode anisotropy.

598 **5.4 Anisotropy Beneath Archean Cratons**

599 Fig. 11 focuses on Archean cratons as defined in model 3SMAC [*Nataf and Ricard*,
600 1996]. Panels (a) and (d) of Fig. 11 display averaged SV and SH amplitude profiles,
601 panels 10(b) and 10(e) show the vertical auto-correlation for SV and SH fast axes, and
602 panels 10(c) and 10(f) represent the angular difference between the APM and the SV fast
603 axes. To calculate the vertical auto-correlation in a specific region, we isolated the
604 targeted area by setting all other regions to zero before performing a generalized
605 spherical harmonics expansion, and amplitudes were scaled so that the auto-correlation
606 functions reflect vertical changes in fast axes and not in amplitude. As for the global
607 average shown in section 5.1, we used Eq. (34) with a 40 km window to calculate vertical
608 auto-correlation curves.

609 The top panels of Fig. 11 are for all Archean cratons averaged together and the bottom
610 panels are for the North American craton, which is sufficiently large for our data to
611 resolve without significant contamination from other tectonic regions. As for oceanic
612 plates, the APM was calculated in the no-net rotation reference frame [*Gripp and*
613 *Gordon*, 2002]. In their regional study of the North American craton, [*Yuan and*
614 *Romanowicz*, 2010] showed that their anisotropy fast axis directions were in better

615 agreement with the APM in the hotspot reference frame than in the no-net rotation
616 reference frame. On the contrary, *Yuan and Beghein* [2013] showed that NNR-NUVEl1
617 gives the best results for all cratons averaged together. This difference in the results is
618 likely linked to the difference in lateral resolutions of the models, which was higher in the
619 regional *Yuan and Romanowicz* [2010] study.

620 As explained by *Yuan and Romanowicz* [2010], constraining the depth of the cratonic
621 lithosphere has long been challenging. While estimates from isotropic velocity models
622 can exceed 300 km [*Grand*, 1994], studies based on body wave conversion or receiver
623 function analyses detect a seismic wave discontinuity at shallow depths around ~100-140
624 km [*Abt et al.*, 2010; *Rychert and Shearer*, 2009]. Radial anisotropy and SV azimuthal
625 anisotropy models, however, yield LAB depths of ~250 km, in closer agreement with
626 results from other types of data such as thermobarometry, heat flow measurements, and
627 electrical conductivity [*Gung et al.*, 2003; *Yuan and Romanowicz*, 2010]. Following *Yuan*
628 *and Romanowicz* [2010], we used the depth at which the SV fast axes change direction
629 and becomes aligned with the APM to determine the LAB depth. This proxy for the LAB
630 depth is justified if we assume that strong horizontal shear associated with plate motion is
631 present in the asthenosphere and aligns olivine fast axes in the direction of mantle flow.
632 This change in anisotropy fast axes corresponds to a low in the auto-correlation function,
633 equivalent to a high gradient in the fast axes direction, and an amplitude minimum. With
634 this method we thus estimated an average LAB depth beneath Archean cratons of 250 km
635 (Fig. 11(a) and (b)). A similar value is obtained from the analysis of SV anisotropy
636 beneath the North American craton (Fig. 11(d) and (e)). This is consistent with *Yuan and*
637 *Romanowicz* [2010]'s regional study of the North American craton, and here we show

638 that this is valid on average for all cratons. Interestingly, we also find that the LAB not
639 only corresponds to a change in SV anisotropy, but is also associated with a change in SH
640 anisotropy, which displays a minimum in amplitude (Fig. 11(a) and (d)) and in the
641 vertical auto-correlation function (Fig. 11(b) and (e)).

642 Several peaks in SH and SV anisotropy amplitudes are visible within this anisotropically
643 defined lithosphere. For all the cratons averaged together, we detect an amplitude
644 minimum in both types of anisotropy between 50 km and 100 km depth, coinciding with
645 a peak in the vertical auto-correlation functions. Another minimum in amplitude and a
646 peak in the vertical auto-correlation is also found around 140 km for SH waves and 180
647 km depth for SV waves. We also find changes in SV fast direction around 50 km and 150
648 km depth beneath the North American craton, but SH anisotropy displays more changes
649 (at ~50 km, 120 km, and 180 km). We tested the robustness of these peaks and troughs in
650 dlnE at a few grid cells beneath continental regions and beneath the northeastern Pacific
651 (Fig. S6). We showed that their position does not significantly change with the spline
652 functions spacing, although if the spacing is too wide the model becomes vertically
653 smoother and we lose some of the model features. In addition, we tested that the presence
654 of the peaks does not strongly depend on the crustal model. This was done by comparison
655 of our results with results obtained using the PREM crust instead of CRUST2.0. This
656 includes an example at a grid cell beneath Tibet, which offers an end-member case as the
657 Moho depth in that region differs significantly from the PREM Moho. Finally, we tested
658 that the presence of discontinuities in the PREM mantle at 80 km and 220 km depth did
659 not affect our results by smoothing the sensitivity kernels at these depths.

660 In their study of North America, *Yuan and Romanowicz* [2010] revealed a similar change
661 in SV anisotropy within the continental lithosphere, which the authors related to chemical
662 layering under the Archaean crust as evidenced by studies of xenoliths and xenocrysts.
663 They also showed that this intra-continental boundary coincides with the depth of the
664 shallow boundary detected by receiver function and body wave conversion studies. Here
665 we detected multiple changes in SV and SH anisotropy within the cratonic lithosphere.
666 The comparison with the results of *Yuan and Romanowicz* [2010] is however not
667 straightforward and we do not attempt to explain the observed anisotropy changes in
668 terms of internal boundaries at this stage. Trade-offs in the model parameters in the top
669 200 km of the mantle (see section 3 for SH anisotropy and *Yuan and Beghein* [2013] for
670 SV anisotropy) imply that our data may not be able to resolve the different peaks in the
671 auto-correlation function. In addition, we are averaging our models over large regions,
672 and lateral variations in the depth of the intermediate boundary as described by *Yuan and*
673 *Romanowicz* [2010] are likely not resolved by our data. More detailed, higher resolution
674 seismological studies of different cratons would be needed to make robust statements
675 regarding the presence of multiple intra-lithospheric boundaries and to compare changes
676 in SH and SV anisotropy within the cratonic lithosphere. Differences are also visible
677 between the SV and SH models at 300 km depth: A low vertical auto-correlation is found
678 for SH anisotropy but not for SV anisotropy. While this could have important
679 geodynamics consequences, the presence of trade-offs among the SH anisotropy
680 parameters in the uppermost mantle casts doubt on whether this difference is significant.

681 **5.5 Spectral Analysis**

682 We expanded YB13SVani and YB14SHani in generalized spherical harmonics up to
683 degree 20 and calculated their power spectra with Eq. (33). Figs. 12 and S7 show the
684 power spectra for the two models at various depths. Because the generalized spherical
685 harmonic expansion of a second order tensor starts at degree 2 (see section 3.2 for details),
686 the SV model power spectrum does not have any power at lower degree. Similarly, the
687 SH model power spectrum does not have any energy at degrees lower than 4 because it
688 results from the generalized spherical harmonic expansion of a fourth order tensor.

689 We observe a decay of $\square_l$ with l for both the 2Ψ and 4Ψ models at most depths, with a
690 loss of power for $l \geq 8$. This is similar to the power spectrum of the SV anisotropy model
691 obtained by *Montagner and Tanimoto* [1991]. This power loss at high degrees may not,
692 however, reflect the actual strength of the anisotropy on Earth, and might instead be
693 related to a loss of resolvable power in the data due to the regularization applied by
694 *Visser et al.* [2008a] during the construction of the phase velocity maps. Indeed, as
695 explained in section 2, the chosen regularization resulted in an estimated resolution of
696 about degree eight for the fundamental modes and about degree six for the higher modes.

697 We detect a dominant degree two in SV anisotropy between ~100 km and ~200 km depth,
698 and in degree four SH anisotropy between ~100 km and ~150 km depth. *Montagner and*
699 *Tanimoto* [1991] had also observed a dominant degree two SV anisotropy at those depths,
700 in addition to a peak in degree six. This, together with the dominance of degree four in
701 their radial anisotropy model, was later interpreted in terms of a simple convection flow
702 pattern by comparison with the corresponding degrees of the hotspots distribution and
703 geoid [*Montagner and Romanowicz*, 1993]. Here, we find a small peak in SV power at
704 degree five instead located at 100 km and 150 km depth, and a peak in degree five SH

anisotropy at 100 km depth. This might indicate a more complex convection pattern than the simple model of *Montagner and Romanowicz* [1993]. To insure that this degree five signal is not due to inadequate crustal corrections, we verified that the power spectrum of the Moho depth does not present a peak at degree five (Fig. S8). We found, however, that this peak in σ_5 can also be found in the power spectra of the 2Ψ terms of the Rayleigh wave phase velocity maps that have sensitivity in the uppermost mantle ($n = 0, 1$, and 2 in Fig. 13(a) and (b)), but are not present in the spectra of data with little sensitivity to these depths ($n = 3$ and $n = 6$ in Fig. 13 (a) and (b)). This demonstrates that the degree five signal is constrained by the phase velocity maps themselves and not due to modeling artifacts on our part.

The strongest power for SV anisotropy is found at 100 km depth for all degrees, and we generally find that most of the SV anisotropy strength is concentrated in the top ~200 km. For SH anisotropy too, the strongest power is located in the top 200 km for degree 5 and higher, but we note a large degree four at 600 km depth as well. The power spectrum at 600 km depth rapidly decreases for higher angular orders. This relatively large degree 4 SH anisotropy in the transition zone is not matched by any particularly large SV anisotropy at any angular degree. Indeed, at 600 km, the SV model has a σ_4 comparable to or lower than that calculated at other depths. This behavior can be found in the Love wave data spectra (Fig. 13(c) and (d)), which show that modes with sensitivity to the transition zone have higher σ_4 than modes with no sensitivity at these depths. We therefore conclude that this signal is contained in the phase velocity data and is unlikely to be due to vertical trade-offs among model parameters.

727 Fig. 14 compares the vertical auto-correlation for SH and SV anisotropy calculated for all
728 degrees of the generalized spherical harmonic expansion, with the vertical auto-
729 correlation of the models truncated at degree eight, and truncated at degree four for SH
730 anisotropy, and degree two for SV anisotropy. We find that the change in SV anisotropy
731 at the top of the MTZ is stronger at degree two, and the change in SH anisotropy is
732 stronger at degree four. This change in fast axes at the MTZ upper boundary is therefore
733 a large-scale signal. We also note differences in the depths of the peaks and troughs of
734 the SH and the SV models, but they are well below the vertical resolution of our model
735 and therefore not significant.

736 **6. CONCLUSIONS**

737 Love wave fundamental and higher mode phase velocity maps were inverted for SH
738 azimuthal anisotropy in the top 800 km of the mantle. We found a general agreement
739 between the average amplitudes of our new SH anisotropy model and the SV azimuthal
740 anisotropy model we previously obtained from Rayleigh wave higher modes [*Yuan and*
741 *Beghein*, 2013], and changes in both SV and SH fast axes generally occur at similar
742 depths. The upper 250 km of the mantle are characterized by average SH and SV
743 anisotropy of ~2%, and we detected ~1% anisotropy for both types of waves in the MTZ.
744 The top of the MTZ is also associated with a change in SV and SH fast axes. Because this
745 is a depth at which the olivine to wadsleyite high-pressure phase change is thought to
746 occur, we inferred that changes in the anisotropic properties of MTZ material are likely at
747 the origin of the observed MTZ signal. The change in fast axes around 410 km depth may
748 result from recrystallization during the phase transformation, a change in slip system, or
749 depth changes in mantle flow direction, which would indicate strong mantle layering.

750 Interpretation of the model in terms of mantle flow and consequences for the
751 thermochemical evolution of the planet are, however, non unique and further mineral
752 physics and geodynamics studies of the anisotropy of MTZ minerals and the effect of
753 pressure, water, or partial melt are needed.

754 Our SV anisotropy model beneath the Pacific and other oceanic plates presents a
755 systematic dependence upon crustal age. It is consistent with a thermal origin of the
756 oceanic LAB beneath the Pacific basin, and the anisotropy of the Pacific asthenosphere is
757 consistent with LPO of olivine due to present-day mantle flow. In contrast, we did not
758 find any relation between the amplitude or fast axes of our new SH anisotropy model
759 with ocean age. Moreover, our results revealed that while uppermost mantle SV
760 anisotropy is anomalously large in the middle of the Pacific plate, as is radial anisotropy,
761 SH anisotropy has amplitudes close to average values for other oceans at this depth. This
762 provides new constraints on the Pacific upper mantle anisotropy signal whose origin has
763 been subject of debate for the past 15 years.

764 Beneath Archean cratons, our results suggest an average LAB depth of ~250 km,
765 consistent with estimates from a regional SV azimuthal anisotropy model of the North
766 American craton [*Yuan and Romanowicz*, 2010]. Here we demonstrated that the cratonic
767 LAB is not only associated with changes in SV anisotropy, but also with changes in SH
768 anisotropy, thereby providing new constraints on the origin of this interface.

769 **7. ACKNOWLEDGMENTS**

770 The data used are the phase velocity maps of *Visser et al.* [2008a], which are readily
771 available on J. Trampert's website at

772 http://www.geo.uu.nl/~jeannot/My_web_pages/Downloads.html. The global anisotropy
773 models are available for download at
774 http://www2.epss.ucla.edu/~cbeghein/Downloads.html. Partial derivatives were
775 calculated using program MINEOS (available on the CIG website at
776 http://www.geodynamics.org/), and figures were made using the Generic Mapping Tool,
777 Gnuplot, and Xmgrace. Improvements to this manuscript were made possible thanks to
778 comments from M. Panning, one anonymous reviewer, and the Associate Editor. Funding
779 for this project came from NSF EAR grants 0838605 and 0949255.

780

781 **8. REFERENCES**
782
783 Abt, D. L., K. M. Fischer, S. W. French, H. A. Ford, H. Yuan, and B. Romanowicz
784 (2010), North American lithospheric discontinuity structure imaged by Psand Spreceiver
785 functions, *J. Geophys. Res.*, *115*(B9), B09301, doi:10.1029/2009JB006914.
786 Anderson, D. L. (1961), Elastic wave propagation in layered anisotropic media, *J.*
787 *Geophys. Res.*, *66*(9), 2953-2963, doi:10.1029/JZ066i009p02953.
788 Backus, G., and F. Gilbert (1968), The Resolving Power of Gross Earth Data, *Geophys. J.*
789 *R. A. S.*, *16*(2), 169-205, doi:10.1111/j.1365-246X.1968.tb00216.x.
790 Bassin, C., G. Laske, and T. G. Masters (2000), The current limits of resolution for
791 surface wave tomography in North America, *Eos Trans. AGU*, *81*(F897).
792 Becker, T. W., G. Ekström, L. Boschi, and J. H. Woodhouse (2007), Length scales,
793 patterns and origin of azimuthal seismic anisotropy in the upper mantle as mapped by
794 Rayleigh waves, *Geophys. J. Int.*, *171*(1), 451-462, doi:10.1111/j.1365-
795 246X.2007.03536.x.
796 Becker, T. W., J. B. Kellogg, G. Ekström, and R. J. O'Connell (2003), Comparison of
797 azimuthal seismic anisotropy from surface waves and finite strain from global mantle‐
798 circulation models, *Geophys. J. Int.*, *155*(2), 696-714, doi:10.1046/j.1365-
799 246X.2003.02085.x.
800 Beghein, C. (2010), Radial anisotropy and prior petrological constraints: A comparative
801 study, *J. Geophys. Res.-Solid Earth*, *115*, doi:10.1029/2008JB005842.
802 Beghein, C., J. Resovsky, and R. D. van der Hilst (2008), The signal of mantle anisotropy
803 in the coupling of normal modes, *Geophys. J. Int.*, *175*(3), 1209-1234,
804 doi:10.1111/j.1365-246X.2008.03970.x.

805 Beghein, C., and J. Trampert (2004), Probability density functions for radial anisotropy:
806 implications for the upper 1200 km of the mantle, *Earth Planet. Sci. Lett.*, *217*(1-2), 151-
807 162, doi:10.1016/S0012-821X(03)00575-2.
808 Beghein, C., J. Trampert, and H. van Heijst (2006), Radial anisotropy in seismic
809 reference models of the mantle, *J. Geophys. Res.-Solid Earth*, *111*(B2),
810 doi:10.1029/2005JB003728.
811 Beghein, C., K. Yuan, N. Schmerr, and Z. Xing (2014), Changes in Seismic Anisotropy
812 Shed Light on the Nature of the Gutenberg Discontinuity, *Science*, *343*(6176), 1237-1240,
813 doi:10.1126/science.1246724.
814 Bevington, P., and K. D. Robinson (2002), *Data Reduction and Error Analysis for the*
815 *Physical Sciences*, 3rd ed., McGraw-Hill, New York, NY.
816 Boschi, L., and G. Ekström (2002), New images of the Earth's upper mantle from
817 measurements of surface wave phase velocity anomalies, *J. Geophys. Res.*, *107*(B4),
818 2059, doi:10.1029/2000JB000059.
819 Boschi, L., and J. H. Woodhouse (2006), Surface wave ray tracing and azimuthal
820 anisotropy: a generalized spherical harmonic approach, *Geophys. J. Int.*, *164*(3), 569-578,
821 doi:10.1111/j.1365-246X.2006.02870.x.
822 Bozdağ, E., and J. Trampert (2010), Assessment of tomographic mantle models using
823 spectral element seismograms, *Geophys. J. Int.*, *180*(3), 1187-1199, doi:10.1111/j.1365-
824 246X.2009.04468.x.
825 Chevrot, S. b., and V. Monteiller (2009), Principles of vectorial tomography - the effects
826 of model parametrization and regularization in tomographic imaging of seismic
827 anisotropy, *Geophys. J. Int.*, *179*(3), 1726-1736, doi:10.1111/j.1365-246X.2009.04370.x.

828 Debayle, E., B. L. N. Kennett, and K. Priestley (2005), Global azimuthal seismic
829 anisotropy and the unique plate-motion deformation of Australia, *Nature*, *433*(7025),
830 509-512, doi:10.1038/nature03247.
831 Debayle, E., and Y. Ricard (2013), Seismic observations of large-scale deformation at the
832 bottom of fast-moving plates, *Earth Planet. Sci. Lett.*, *376*(C), 165-177,
833 doi:10.1016/j.epsl.2013.06.025.
834 Dziewonski, A. M., and D. L. Anderson (1981), Preliminary reference Earth model, *Phys.*
835 *Earth Planet. Int.*, *25*(4), 297-356, doi:10.1016/0031-9201(81)90046-7.
836 Ekström, G., and A. M. Dziewonski (1998), The unique anisotropy of the Pacific upper
837 mantle, *Nature*, *394*(6689), 168-172, doi:10.1038/28148.
838 Ferreira, A. M. G., K. Visser, J. H. Woodhouse, and J. Trampert (2010), On the
839 robustness of global radially anisotropic surface wave tomography, *J. Geophys. Res.*,
840 *115*(B4), B04313, doi:10.1029/2009JB006716.
841 Foley, B. J., and M. D. Long (2011), Upper and mid-mantle anisotropy beneath the
842 Tonga slab, *Geophys. Res. Lett.*, *38*(2), doi:10.1029/2010GL046021.
843 Fouch, M. J., and K. M. Fischer (1996), Mantle anisotropy beneath northwest Pacific
844 subduction zones, *J. Geophys. Res.-Solid Earth*, *101*(B7), 15987, doi:10.1029/96JB00881.
845 Gaboret, C., A. M. Forte, and J.-P. Montagner (2003), The unique dynamics of the
846 Pacific Hemisphere mantle and its signature on seismic anisotropy, *Earth Planet. Sci.*
847 *Lett.*, *208*(3-4), 219-233, doi:10.1016/S0012-821X(03)00037-2.
848 Grand, S. P. (1994), Mantle shear structure beneath the Americas and surrounding oceans,
849 *J. Geophys. Res.*, *99*(B6), 11591-11531, doi:10.1029/94JB00042.

850 Gripp, A. E., and R. G. Gordon (2002), Young tracks of hotspots and current plate
851 velocities, *Geophys. J. Int.*, *150*(2), 321-361, doi:10.1046/j.1365-246X.2002.01627.x.
852 Gung, Y., M. P. Panning, and B. Romanowicz (2003), Global anisotropy and the
853 thickness of continents, *Nature*, *422*(6933), 707-711, doi:10.1038/nature01559.
854 Hess, H. (1964), Seismic Anisotropy of the Uppermost Mantle under Oceans, *Nature*,
855 *203*(4945), 629-631, doi:10.1038/203629a0.
856 Ismaı□l, W. B., and D. Mainprice (1998), An olivine fabric database: an overview of
857 upper mantle fabrics and seismic anisotropy, *Tectonophysics*, *296*(1-2), 145-157,
858 doi:10.1016/S0040-1951(98)00141-3.
859 Jackson, D. D. (1972), Interpretation of inaccurate, insufficient and inconsistent data,
860 *Geophys. J. R. A. S.*, *28*(2), 97-109, doi:10.1111/j.1365-246X.1972.tb06115.x.
861 Jung, H., and S.-i. Karato (2001), Water-Induced Fabric Transitions in Olivine, *Science*,
862 *293*(5534), 1460-1463, doi:10.1126/science.1062235.
863 Karato, S.-I. (1989), Seismic anisotropy: Mechanisms and tectonic implications, in
864 *Rheology of Solids and of the Earth*, edited by S.-i. Karato and M. Toriumi, pp. 393–422,
865 Oxford University Press, New York.
866 Kawazoe, T., T. Ohuchi, Y. Nishihara, N. Nishiyama, K. Fujino, and T. Irifune (2013),
867 Seismic anisotropy in the mantle transition zone induced by shear deformation of
868 wadsleyite, *Physics Earth Planet. Int.*, *216*(C), 91-98, doi:10.1016/j.pepi.2012.12.005.
869 Kendall, J. M., and P. G. Silver (1996), Constraints from seismic anisotropy on the nature
870 of the lowermost mantle, *Nature*, *381*(6581), 409-412, doi:10.1038/381409a0.
871 Kustowski, B., A. M. Dziewonski, and G. Ekström (2007), Nonlinear Crustal Corrections
872 for Normal-Mode Seismograms, *BSSA*, *97*(5), 1756-1762, doi:10.1785/0120070041.

873 Kustowski, B., G. Ekström, and A. M. Dziewonski (2008), Anisotropic shear-wave
874 velocity structure of the Earth's mantle: A global model, *J. Geophys. Res.*, *113*(B6),
875 B06306, doi:10.1029/2007JB005169.
876 Lanczos, C. (1961), *Linear Differential Operators*, 564 pp., D. Van Nostrand Reinhold
877 Co., London.
878 Lekić, V., and M. P. Panning (2010), A simple method for improving crustal corrections
879 in waveform tomography, *Geophys. J. Int.*, doi:10.1111/j.1365-246X.2010.04602.x.
880 Love, A. E. H. (1927), *A treatise on the mathematical theory of elasticity*, Cambridge
881 University Press, Cambridge.
882 Marone, F., and B. Romanowicz (2007), Non-linear crustal corrections in high-resolution
883 regional waveform seismic tomography, *Geophys. J. Int.*, *170*(1), 460-467,
884 doi:10.1111/j.1365-246X.2007.03399.x.
885 Matsu'Ura, M., and N. Hirata (1982), Generalized least-squares solutions to quasi-linear
886 inverse problems with a priori information, *J. Phys. Earth*, *30*(6), 451-468,
887 doi:10.4294/jpe1952.30.451.
888 Menke, W. (1989), *Geophysical Data Analysis: Discrete Inverse Theory*, 289 pp.,
889 Academic Press, San Diego, CA.
890 Miyazaki, T., K. Sueyoshi, and T. Hiraga (2013), Olivine crystals align during diffusion
891 creep of Earth's upper mantle, *Nature*, *502*(7471), 321-326, doi:10.1038/nature12570.
892 Montagner, J.-P., and B. L. N. Kennett (1996), How to reconcile body-wave and normal-
893 mode reference earth models, *Geophys. J. Int.*, *125*(1), 229-248, doi:10.1111/j.1365-
894 246X.1996.tb06548.x.

895 Montagner, J.-P., and H. C. Nataf (1986), A Simple Method for Inverting the Azimuthal
896 Anisotropy of Surface-Waves, *J. Geophys. Res.*, *91*(B1), 511-520,
897 doi:10.1029/JB091iB01p00511.
898 Montagner, J.-P., and B. Romanowicz (1993), Degrees 2, 4, 6 inferred from seismic
899 tomography, *Geophys. Res. Lett.*, *20*(7), 631-634, doi:10.1029/92GL01204.
900 Montagner, J.-P., and T. Tanimoto (1990), Global Anisotropy in the Upper Mantle
901 Inferred From the Regionalization of Phase Velocities, *J. Geophys. Res.*, *95*(B4), 4797-
902 4819, doi:10.1029/JB095iB04p04797.
903 Montagner, J.-P., and T. Tanimoto (1991), Global Upper Mantle Tomography of Seismic
904 Velocities and Anisotropies, *J. Geophys. Res.*, *96*(B12), 20337-20351,
905 doi:10.1029/91JB01890.
906 Nataf, H. C., and Y. Ricard (1996), 3SMAC: an a priori tomographic model of the upper
907 mantle based on geophysical modeling, *Phys. Earth Planet. Int.*, *95*(1-2), 101-122,
908 doi:10.1016/0031-9201(95)03105-7.
909 Nettles, M., and A. M. Dziewonski (2008), Radially anisotropic shear velocity structure
910 of the upper mantle globally and beneath North America, *J. Geophys. Res.*, *113*(B2),
911 B02303, doi:10.1029/2006JB004819.
912 Nicolas, A., and N. I. Christensen (2013), Formation of Anisotropy in Upper Mantle
913 Peridotites - A Review, in Composition, Structure and Dynamics of the Lithosphere-
914 Asthenosphere System, in *Geodynamics Series*, edited by K. Fuchs and C. Froidevaux,
915 AGU, Washington, D. C., doi:10.1029/GD016p0111.

916 Nishimura, C. E., and D. W. Forsyth (1989), The Anisotropic Structure of the Upper
917 Mantle in the Pacific, *Geophys. J.*, *96*(2), 203-229, doi:10.1111/j.1365-
918 246X.1989.tb04446.x.
919 Oganov, A. R., R. Martoňák, A. Laio, P. Raiteri, and M. Parrinello (2005), Anisotropy of
920 Earth's D″ layer and stacking faults in the MgSiO3 post-perovskite phase, *Nature*,
921 *438*(7071), 1142-1144, doi:10.1038/nature04439.
922 Panning, M. P., and B. Romanowicz (2004), Inferences on Flow at the Base of Earth's
923 Mantle Based on Seismic Anisotropy, *Science*, *303*(5656), 351-353,
924 doi:10.1126/science.1091524.
925 Panning, M. P., and B. Romanowicz (2006), A three-dimensional radially anisotropic
926 model of shear velocity in the whole mantle, *Geophys. J. Int.*, *167*(1), 361-379,
927 doi:10.1111/j.1365-246X.2006.03100.x.
928 Parker, R. L., and D. W. Oldenburg (1973), Thermal model of ocean ridges, *Nature*,
929 *242*(122), 137-139, doi:10.1038/physci242137a0.
930 Phinney, R. A., and R. Burridge (1973), Representation of the elastic‐gravitational
931 excitation of a spherical earth model by generalized spherical harmonics, *Geophys. J.*
932 *R.A.S.*, *34*(4), 451-487, doi:10.1111/j.1365-246X.1973.tb02407.x.
933 Rychert, C. A., and P. M. Shearer (2009), A Global View of the Lithosphere-
934 Asthenosphere Boundary, *Science*, *324*(5926), 495-498, doi:10.1126/science.1169754.
935 Sambridge, M. (1999a), Geophysical inversion with a neighbourhood algorithm-II.
936 Appraising the ensemble, *Geophys. J. Int.*, *138*(3), 727-746, doi:10.1046/j.1365-
937 246x.1999.00900.x.

938 Sambridge, M. (1999b), Geophysical inversion with a neighbourhood algorithm—I.
939 Searching a parameter space, *Geophys. J. Int.*, *138*(2), 479-494, doi:10.1046/j.1365-
940 246X.1999.00876.x.
941 Sieminski, A., Q. Liu, J. Trampert, and J. Tromp (2007), Finite-frequency sensitivity of
942 surface waves to anisotropy based upon adjoint methods, *Geophys. J. Int.*, *168*(3), 1153-
943 1174, doi:10.1111/j.1365-246X.2006.03261.x.
944 Silver, P. G. (1996), Seismic anisotropy beneath the continents: Probing the depths of
945 geology*, Annu. Rev. Earth Planet. Sci.*, *24*, 385-432, doi:10.1146/annurev.earth.24.1.385.
946 Smith, D. B., M. H. Ritzwoller, and N. M. Shapiro (2004), Stratification of anisotropy in
947 the Pacific upper mantle, *J. Geophys. Res.*, *109*(B11), B11309,
948 doi:10.1029/2004JB003200.
949 Snieder, R., and J. Trampert (2000), Linear and Nonlinear Inverse Problems, in *Geomatic*
950 *Method for the Analysis of Data in the Earth Sciences*, edited by A. Dermanis, A. Grün
951 and F. Sansò, pp. 93-164, Springer Berlin Heidelberg, doi:10.1007/3-540-45597-3_3.
952 Takeuchi, H., and M. Saito (1972), Seismic surface waves, in *Methods in Computational*
953 *Physics*, edited by B. A. Bolt, pp. 217- 295, Academic Press, New York.
954 Tommasi, A., D. Mainprice, P. Cordier, C. Thoraval, and H. Couvy (2004), Strain-
955 induced seismic anisotropy of wadsleyite polycrystals and flow patterns in the mantle
956 transition zone, *J. Geophys. Res.*, *109*(B12), B12405, doi:10.1029/2004JB003158.
957 Trampert, J., and H.-J. van Heijst (2002), Global Azimuthal Anisotropy in the Transition
958 Zone, *Science*, *296*(5571), 1297-1299, doi:10.1126/science.1070264.

959 Trampert, J., and J. H. Woodhouse (2003), Global anisotropic phase velocity maps for
960 fundamental mode surface waves between 40 and 150 s, *Geophys. J. Int.*, *154*(1), 154-
961 165, doi:10.1046/j.1365-246X.2003.01952.x.
962 Visser, K., J. Trampert, and B. L. N. Kennett (2008a), Global anisotropic phase velocity
963 maps for higher mode Love and Rayleigh waves, *Geophys. J. Int.*, *172*(3), 1016-1032,
964 doi:10.1111/j.1365-246X.2007.03685.x.
965 Visser, K., J. Trampert, S. Lebedev, and B. L. N. Kennett (2008b), Probability of radial
966 anisotropy in the deep mantle, *Earth Planet. Sci. Lett.*, *270*(3-4), 241-250,
967 doi:10.1016/j.epsl.2008.03.041.
968 Wang, N., J.-P. Montagner, A. Fichtner, and Y. Capdeville (2013), Intrinsic versus
969 extrinsic seismic anisotropy: The radial anisotropy in reference Earth models, *Geophys.*
970 *Res. Lett.*, *40*(16), 4284-4288, doi:10.1002/grl.50873.
971 Wiggins, R. A. (1972), The general linear inverse problem: Implication of surface waves
972 and free oscillations for Earth structure, *Rev. Geophys.*, *10*(1), 251-235,
973 doi:10.1029/RG010i001p00251.
974 Wookey, J., J.-M. Kendall, and G. Barruol (2002), Mid-mantle deformation inferred from
975 seismic anisotropy, *Nature*, *415*(6873), 777-780, doi:10.1038/415777a.
976 Yuan, H., and B. Romanowicz (2010), Lithospheric layering in the North American
977 craton, *Nature*, *466*(7310), 1063-1068, doi:10.1038/nature09332.
978 Yuan, K., and C. Beghein (2013), Seismic anisotropy changes across upper mantle phase
979 transitions, *Earth Planet. Sci. Lett.*, *374*, 132-144, doi:10.1016/j.epsl.2013.05.031.
980 Zha, C., T. S. Duffy, H. Mao, R. T. Downs, R. J. Hemley, and D. J. Weidner (1997),
981 Single-crystal elasticity of β-Mg_2SiO_4 to the pressure of the 410 km seismic discontinuity

in the Earth's mantle, *Earth Planet. Sci. Lett.*, *147*(1-4), E9-E15, doi:10.1016/S0012-821X(97)00010-1.

Zhang, S., and S.-i. Karato (1995), Lattice preferred orientation of olivine aggregates deformed in simple shear, *Nature*, *375*(6534), 774-777, doi:10.1038/375774a0.

Figure 1: Sensitivity kernels calculated using PREM [*Dziewoński and Anderson*, 1981] for elastic parameter E with respect to N ($N = \rho V_{SH}^2$) for all the modes used in this study. Each line corresponds to one of the modes employed.

Figure 2: Cubic spline functions used to parameterize the model vertically. The spacing between them is 50 km in the top 300 km and 100 km spacing at larger depths. The dashed curve highlights the shape of a single spline with a peak at 150 km depth.

Figure 3: Synthetic tests with input models (thin dotted curves) simulating azimuthal anisotropy layers of 60 km ((a) and (b)), 80 km ((c) and (d)), 100 km ((e) and (f)), and 120 km ((g) and (h)) thickness. The input amplitude decreases with depth and the input model fast axes change by 45° from one layer to the next. The output models were obtained using the same data uncertainties as for the real data inversions, and the same level of regularization as that chosen for our "preferred" model. The thick solid line represents the output model obtained without adding noise to the synthetic data. The thick dashed line and the thin solid line are for an output models obtained with noise in the data as detailed in the main text.

Figure 4: Model resolution matrix. The numbers indicate the different spline parameters (Eqs. (6) and (7)).

Figure 5: Averaged reduced χ^2 for different trace of resolution matrix obtained by changing the prior model covariance (section 3.1). The reduced χ^2 was calculated for a model with anisotropy in the top 410 km (model A), in the top 670 km (model B) and our SH anisotropy model YB14SHani. The squares mark the regularization chosen for the F-tests.

Figure 6: Root mean square relative SH anisotropy amplitude (a) compared to the SV anisotropy amplitude of models YB13SVani [*Yuan and Beghein*, 2013], DKP2005 [*Debayle et al*., 2005], and DR2013 {*Debayle and Ricard*, 2013} (c), and global vertical auto-correlation for the 4ψ (b) and the 2ψ (d) models expanded in generalized spherical harmonics up to degree 20. The thick horizontal dashed line shows changes in SH and SV anisotropy near the top of the MTZ.

Figure 7: Lateral variations in SH anisotropy at different depths. The crosses show the fast propagation direction and their length is proportional to the amplitude of the anisotropy. The background grey scale is also indicative of the anisotropy relative amplitude. White lines represent the plate boundaries and black lines are for coastlines. The maximum anisotropy amplitude is displayed on the top of each panel.

Figure 8: Lateral variations in SV anisotropy [*Yuan and Beghein*, 2013] at different depths. The bars show the fast propagation direction and their length is proportional to the amplitude of the anisotropy. The background grey scale is also indicative of the anisotropy relative amplitude. White lines represent the plate boundaries, black lines are for coastlines, and arrows display the APM direction calculated using NNR-NUVEL 1A [*Gripp and Gordon*, 2002]. The maximum anisotropy amplitude is displayed on the top of each panel.

Figure 9: Average amplitude for E/N (left, this model) and G/L (middle, *Yuan and Beghein* [2013]), and angular difference between the APM and SV fast axes (right, *Yuan and Beghein* [2013]) for all oceans (top), all oceans minus the Pacific plate (middle row), and for the Pacific plate only (bottom) calculated for different oceanic crust ages.

Figure 10: Uppermost mantle relative SH anisotropy amplitude averaged over the Pacific plate as a function of crustal age. The black solid line represents a half-space cooling model [*Parker and Oldenburg*, 1973] assuming $T_m = 1350$℃ for the mantle temperature, and $\kappa = 10^{-6} m^2 s^{-1}$ for the thermal diffusivity.

Figure 11: (a) and (c) Average amplitude for E/N (this model) and G/L [*Yuan and Beghein*, 2013], (b) and (d) vertical auto-correlation for the 2ψ and 4ψ terms as a function of depth, and (c) and (f) angular difference between the APM and SV fast axes (rightmost panel) beneath all Archean cratons averaged together (top) and the North American craton (bottom) as defined in model 3SMAC [*Nataf and Ricard*, 1996]. The dashed line represents the estimated average depth of the cratonic LAB following *Yuan and Romanowicz* [2011].

Figure 12: Power spectrum calculated up to spherical harmonic degree 20 for model YB13SVani (top) and YB14SHani (this study, bottom) at various depths.

Figure 13: Power spectrum calculated up to spherical harmonic degree 20 for the Rayleigh waves 2Ψ terms (a) and for the Love wave 4Ψ terms (c) and corresponding sensitivity kernels ((b) and (d)).

Figure 14: Vertical auto-correlation function for SH (a) and SV (b) anisotropy calculated for our models expanded up to degree 20 and for truncated expansions of the models.

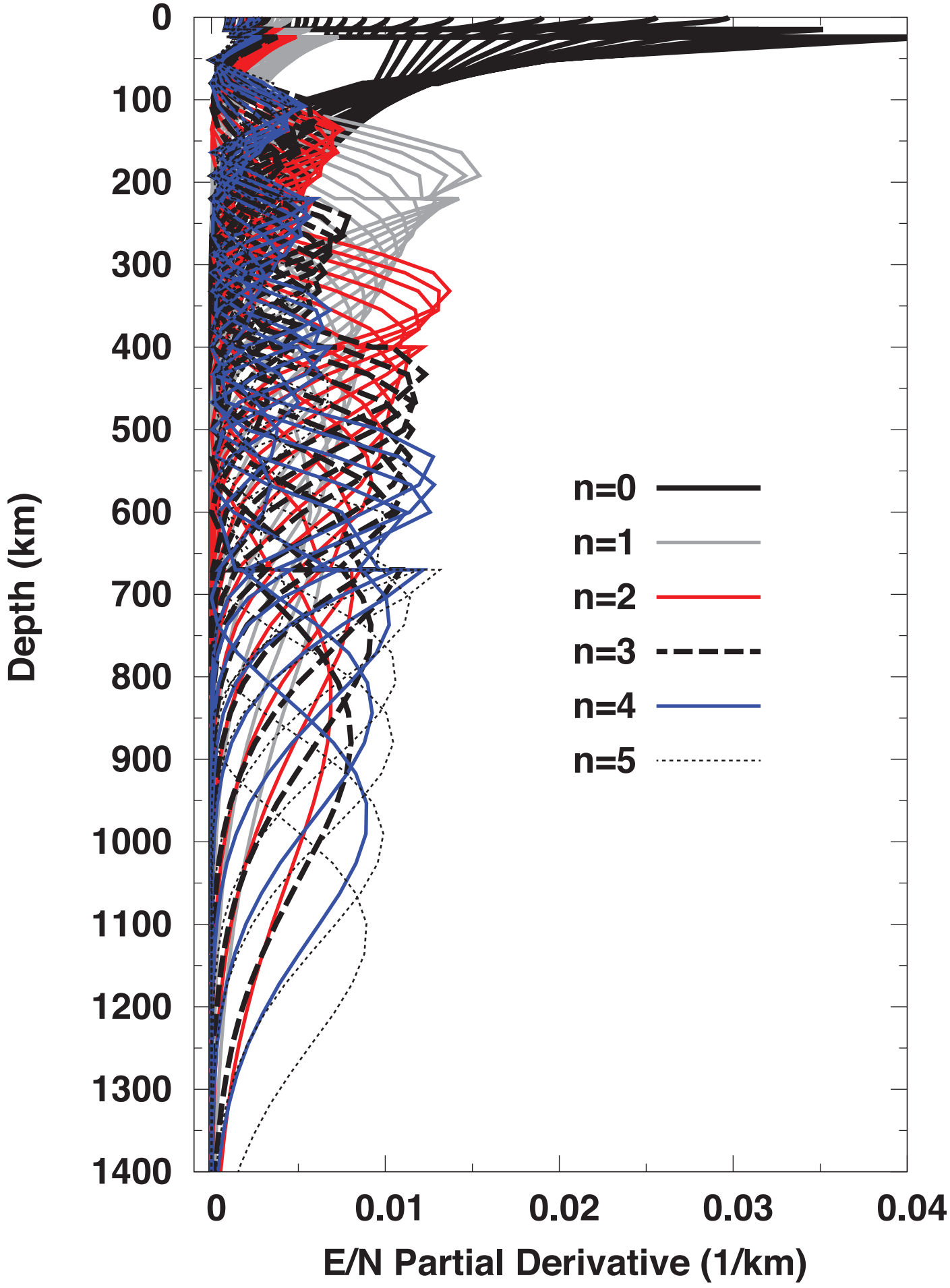
Depth (km)
0
100
200
300
400
500
600
700
800
900
1000
1100
1200
1300
1400
0
0.01
0.02
0.03
0.04
E/N Partial Derivative (1/km)
n=0
n=1
n=2
n=3
n=4
n=5

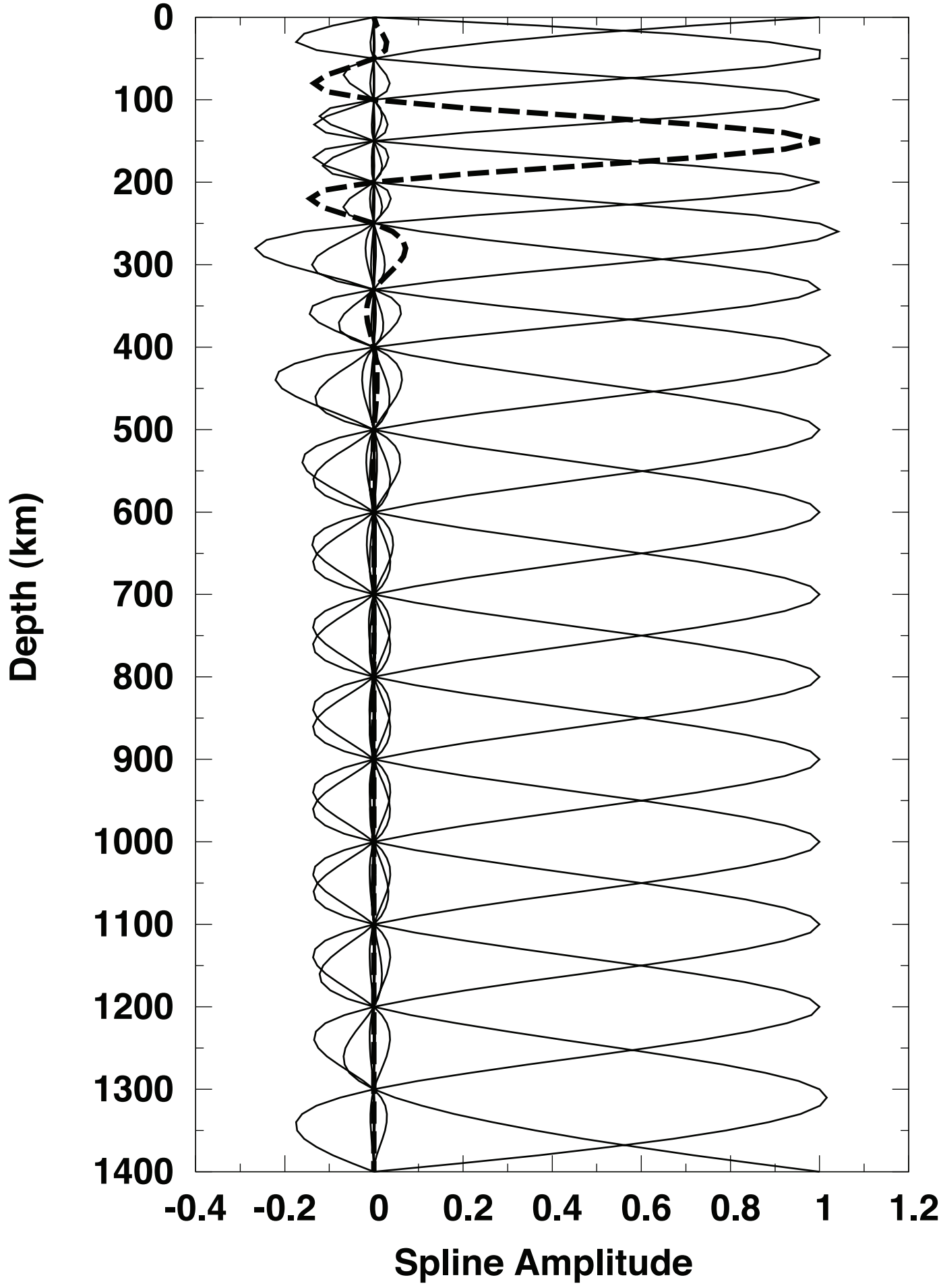
0
100
200
300
400
500
600
700
800
900
1000
1100
1200
1300
1400
Depth (km)
-0.4
-0.2
0
0.2
0.4
0.6
0.8
1
1.2
Spline Amplitude

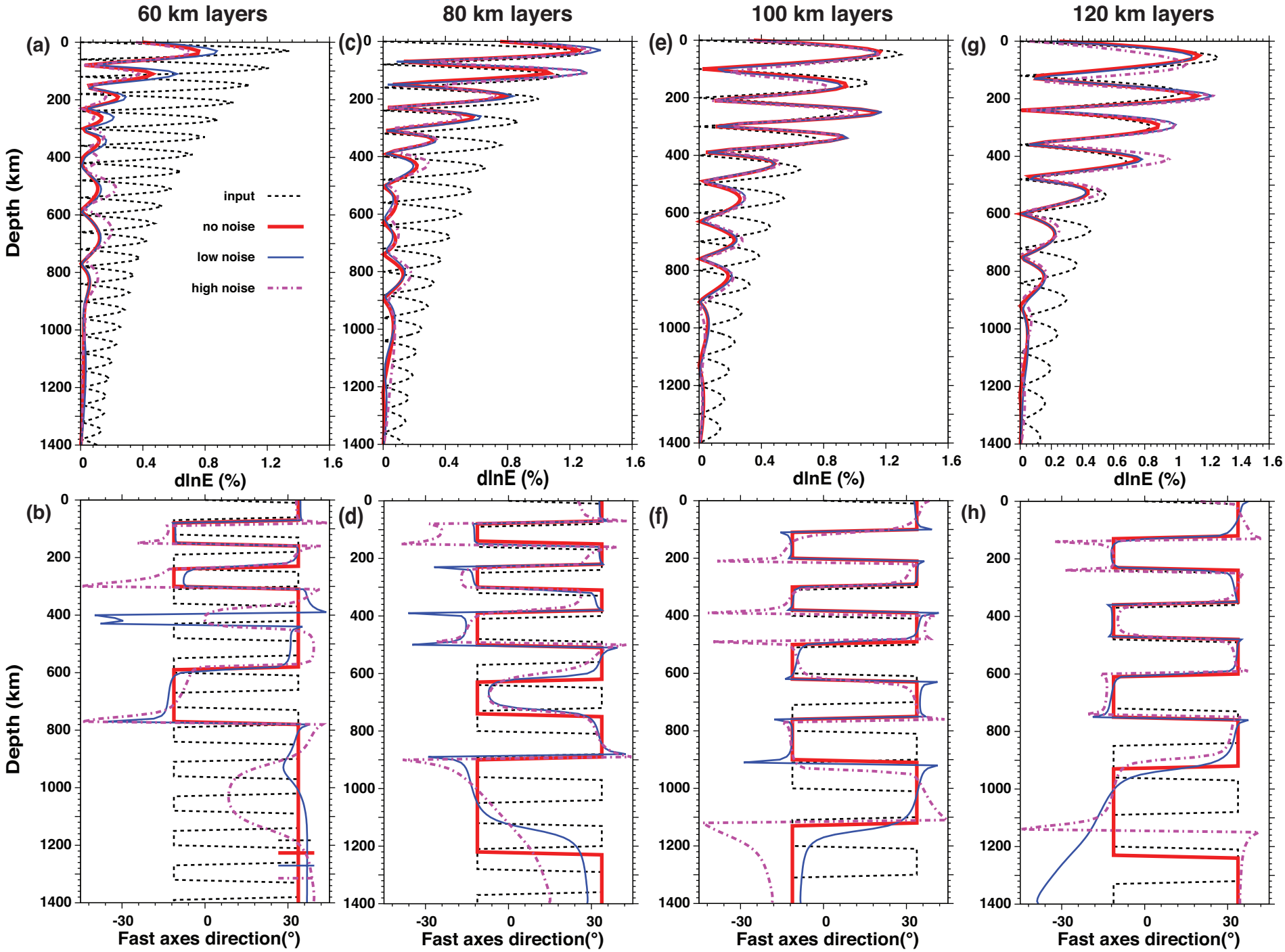
60 km layers
80 km layers
100 km layers
120 km layers
(a)
(b)
(c)
(d)
(e)
(f)
(g)
(h)
Depth (km)
dlnE (%)
Fast axes direction(°)
input
no noise
low noise
high noise

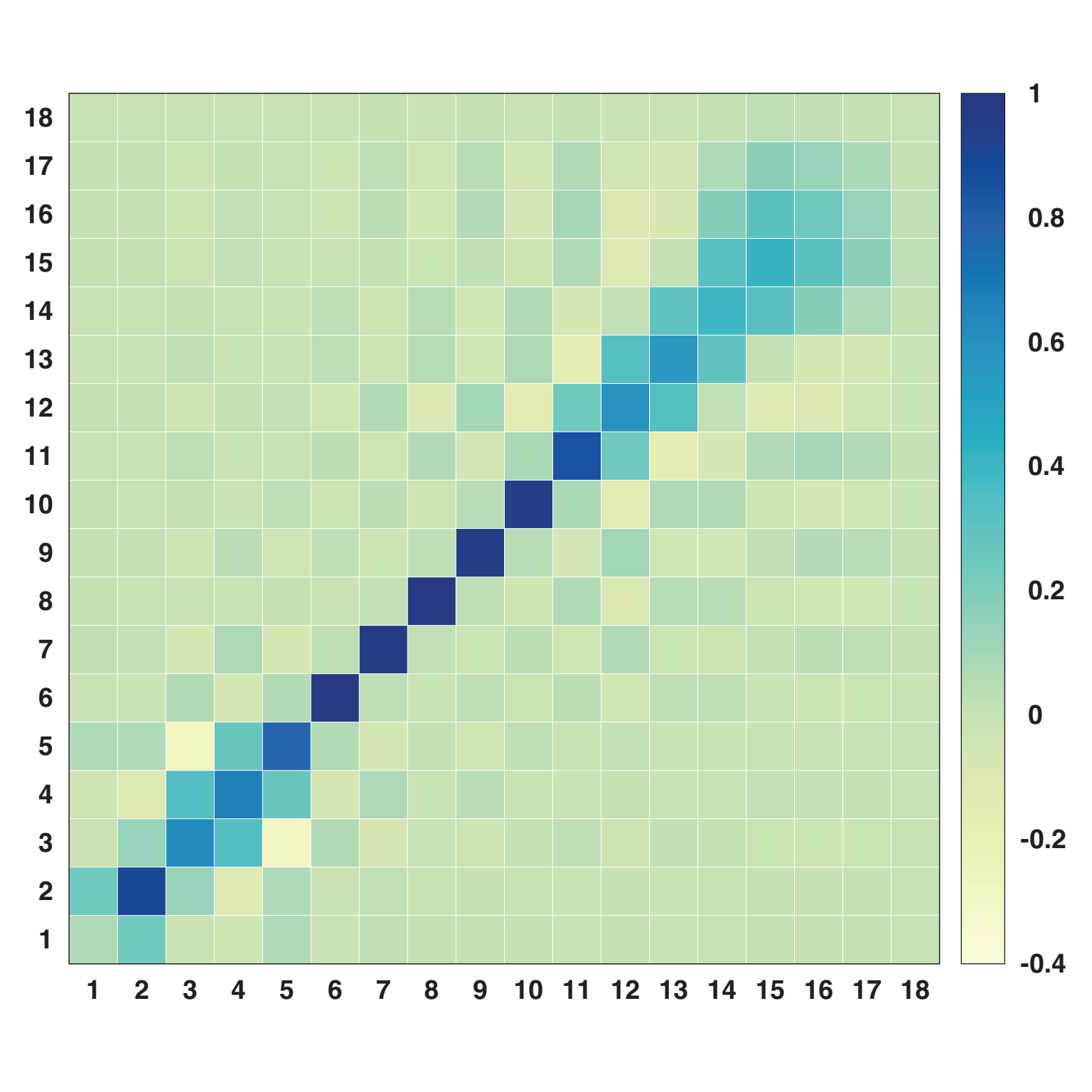
18
17
16
15
14
13
12
11
10
9
8
7
6
5
4
3
2
1
1 2 3 4 5 6 7 8 9 10 11 12 13 14 15 16 17 18
1
0.8
0.6
0.4
0.2
0
-0.2
-0.4

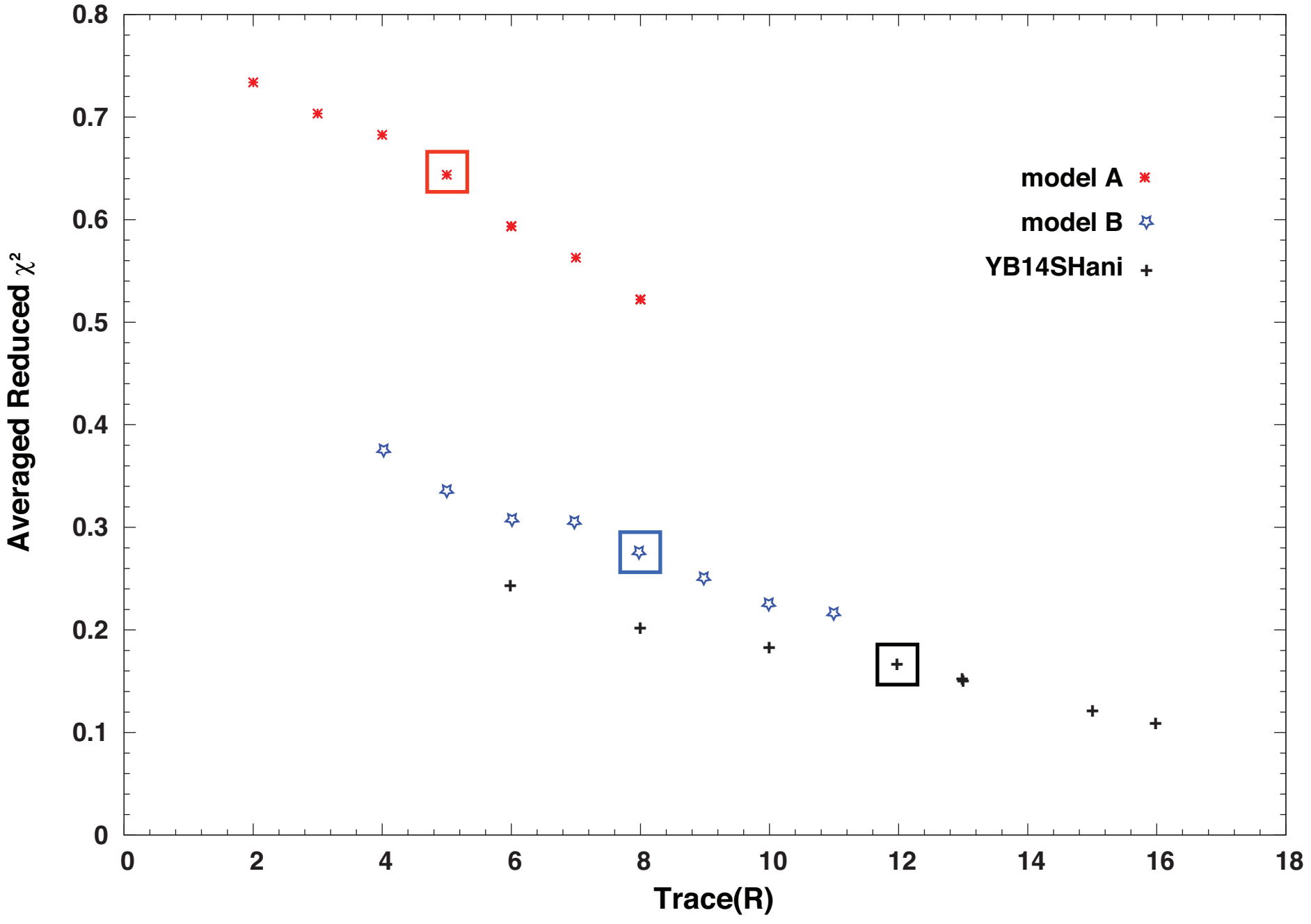
0.8
0.7
0.6
0.5
0.4
0.3
0.2
0.1
0
Averaged Reduced χ^2
0
2
4
6
8
10
12
14
16
18
Trace(R)
model A
model B
YB14SHani

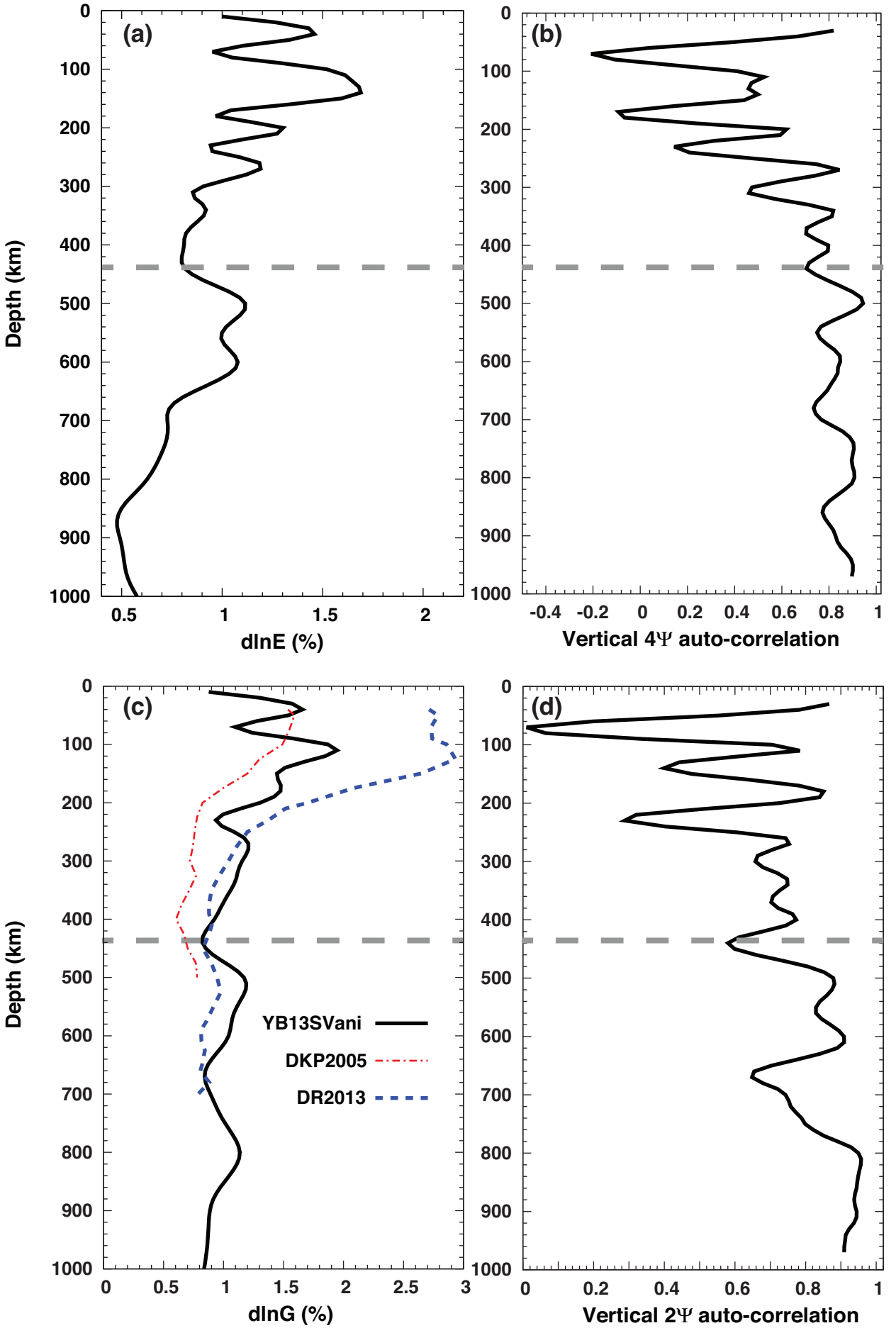
(a)
(b)
(c)
(d)
Depth (km)
dlnE (%)
Vertical 4Ψ auto-correlation
dlnG (%)
Vertical 2Ψ auto-correlation
YB13SVani
DKP2005
DR2013

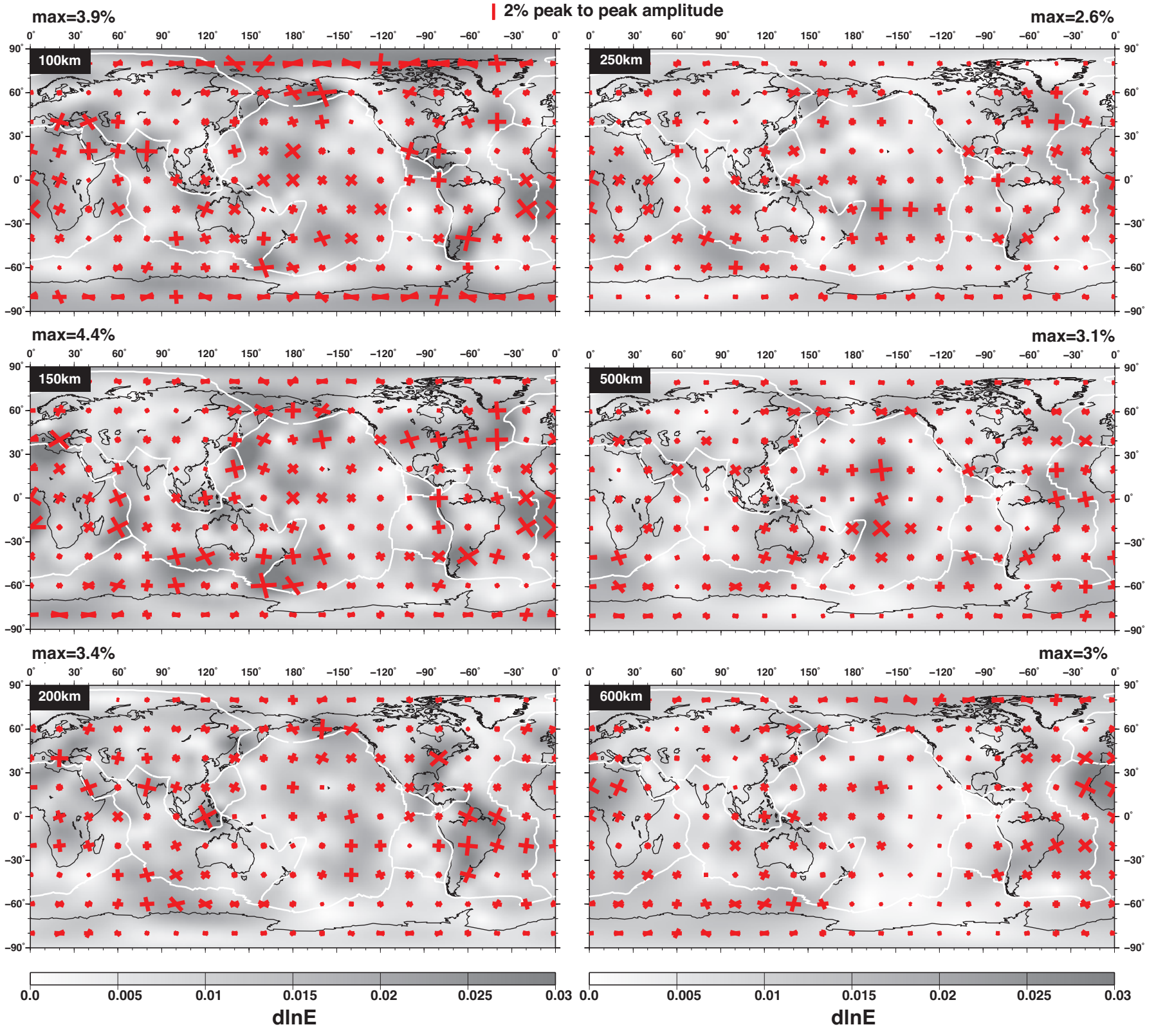
2% peak to peak amplitude
max=3.9%
100km
max=2.6%
250km
max=4.4%
150km
max=3.1%
500km
max=3.4%
200km
max=3%
600km
0° 30° 60° 90° 120° 150° 180° −150° −120° −90° −60° −30° 0°
90° 60° 30° 0° −30° −60° −90°
0.0 0.005 0.01 0.015 0.02 0.025 0.03
dlnE
dlnE

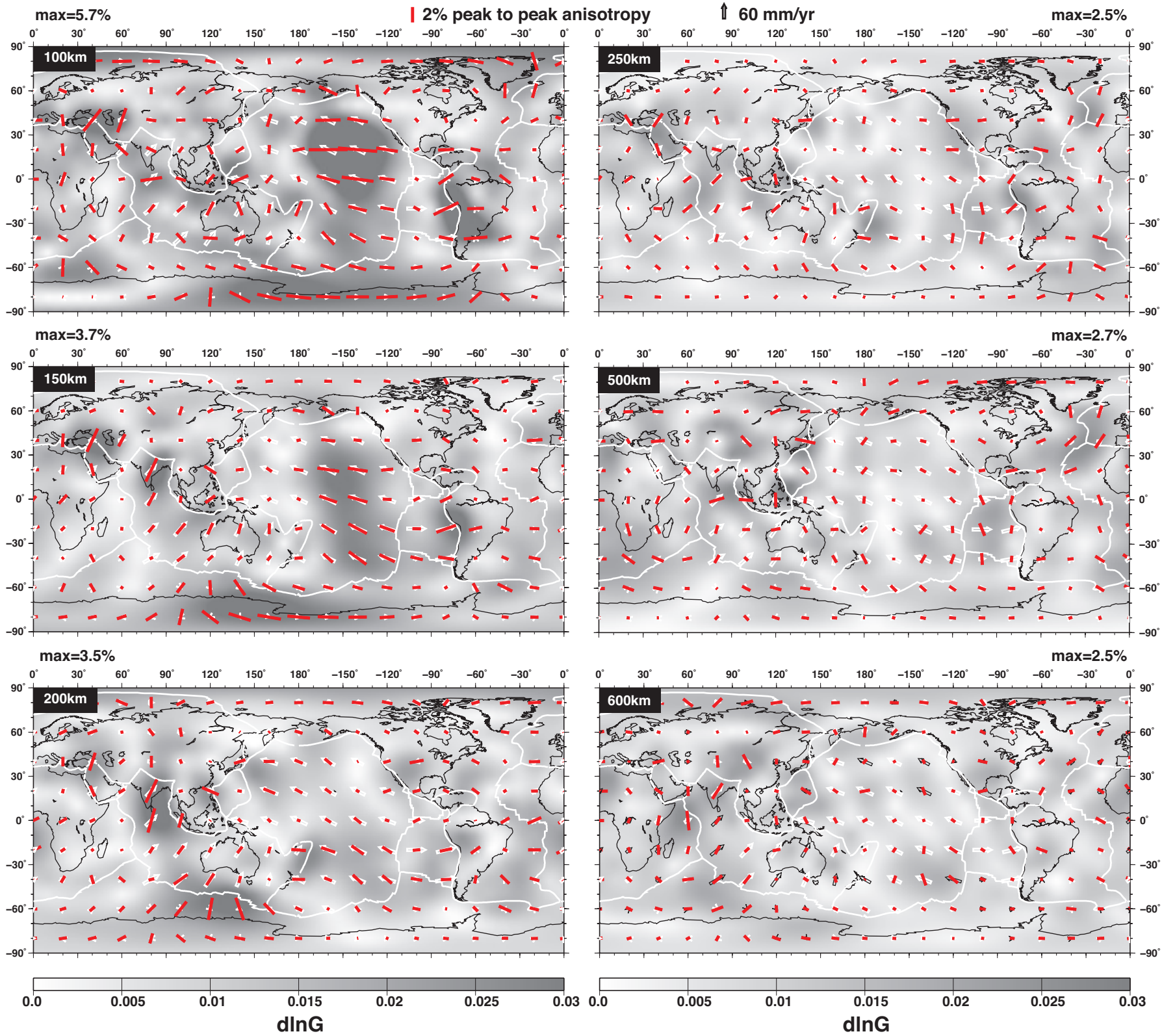
2% peak to peak anisotropy
60 mm/yr
max=5.7%
100km
max=2.5%
250km
max=3.7%
150km
max=2.7%
500km
max=3.5%
200km
max=2.5%
600km
0.0
0.005
0.01
0.015
0.02
0.025
0.03
dlnG
dlnG

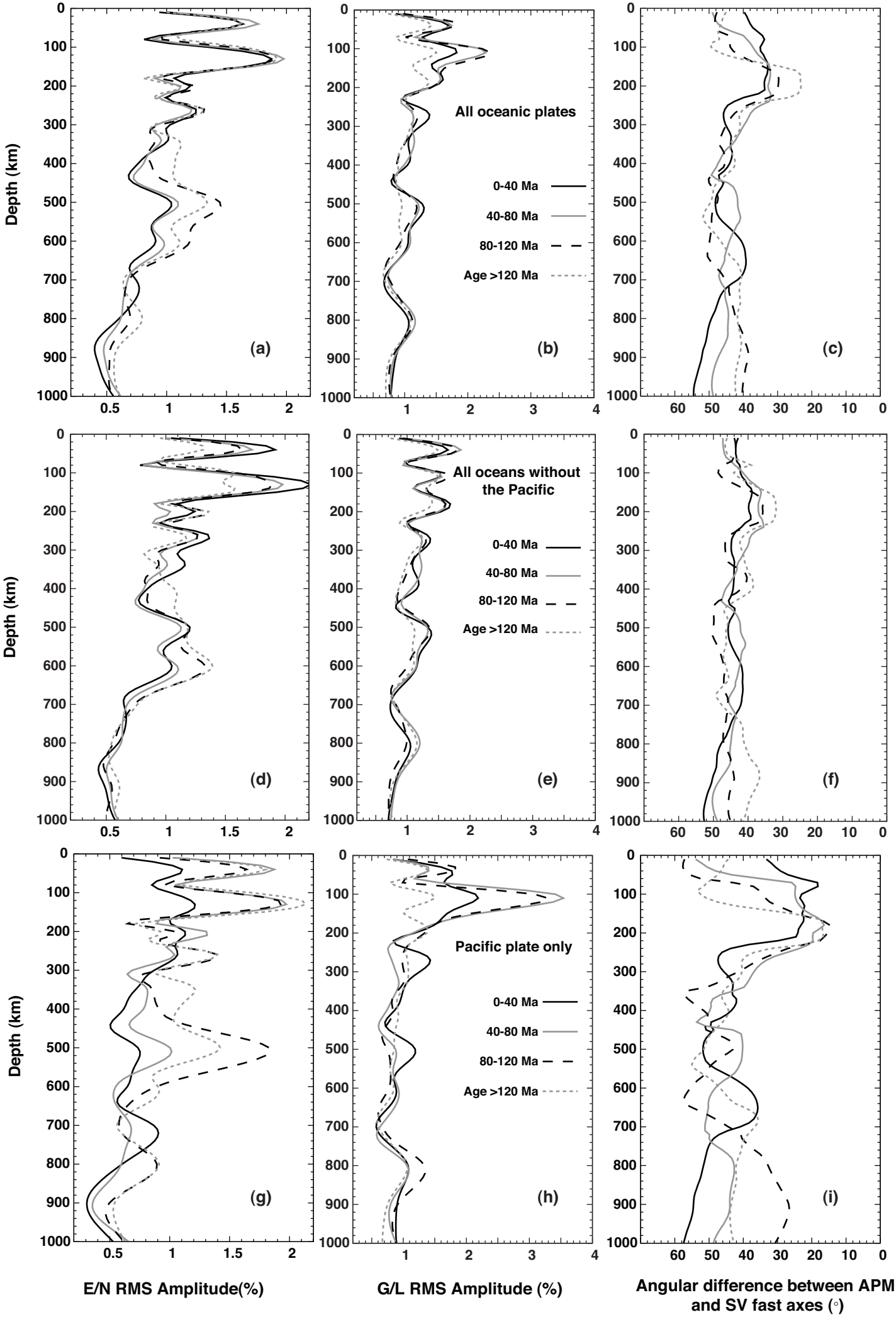
Depth (km)
All oceanic plates
0-40 Ma
40-80 Ma
80-120 Ma
Age >120 Ma
(a)
(b)
(c)
All oceans without the Pacific
(d)
(e)
(f)
Pacific plate only
(g)
(h)
(i)
E/N RMS Amplitude(%)
G/L RMS Amplitude (%)
Angular difference between APM and SV fast axes (◦)

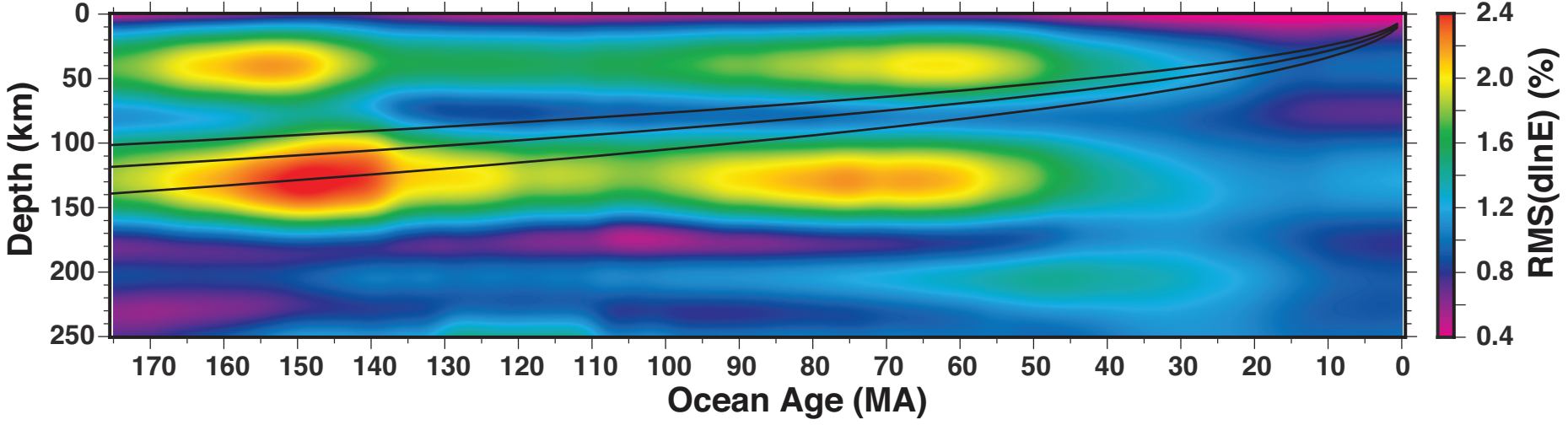
Depth (km)
0
50
100
150
200
250
170
160
150
140
130
120
110
100
90
80
70
60
50
40
30
20
10
0
Ocean Age (MA)
RMS(dlnE) (%)
2.4
2.0
1.6
1.2
0.8
0.4

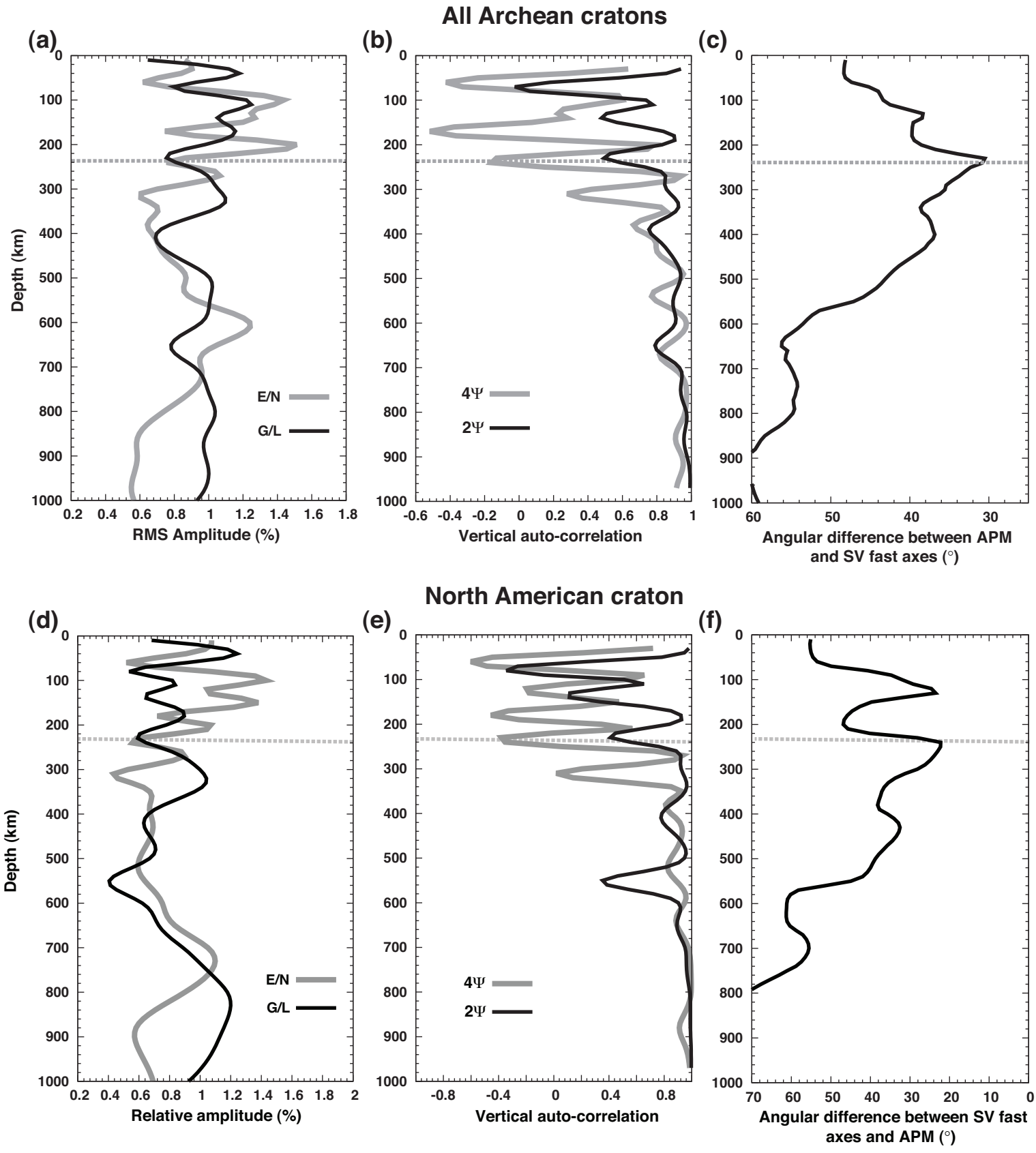
All Archean cratons
(a)
(b)
(c)
Depth (km)
E/N
G/L
RMS Amplitude (%)
4Ψ
2Ψ
Vertical auto-correlation
Angular difference between APM and SV fast axes (°)
North American craton
(d)
(e)
(f)
Relative amplitude (%)
Angular difference between SV fast axes and APM (°)

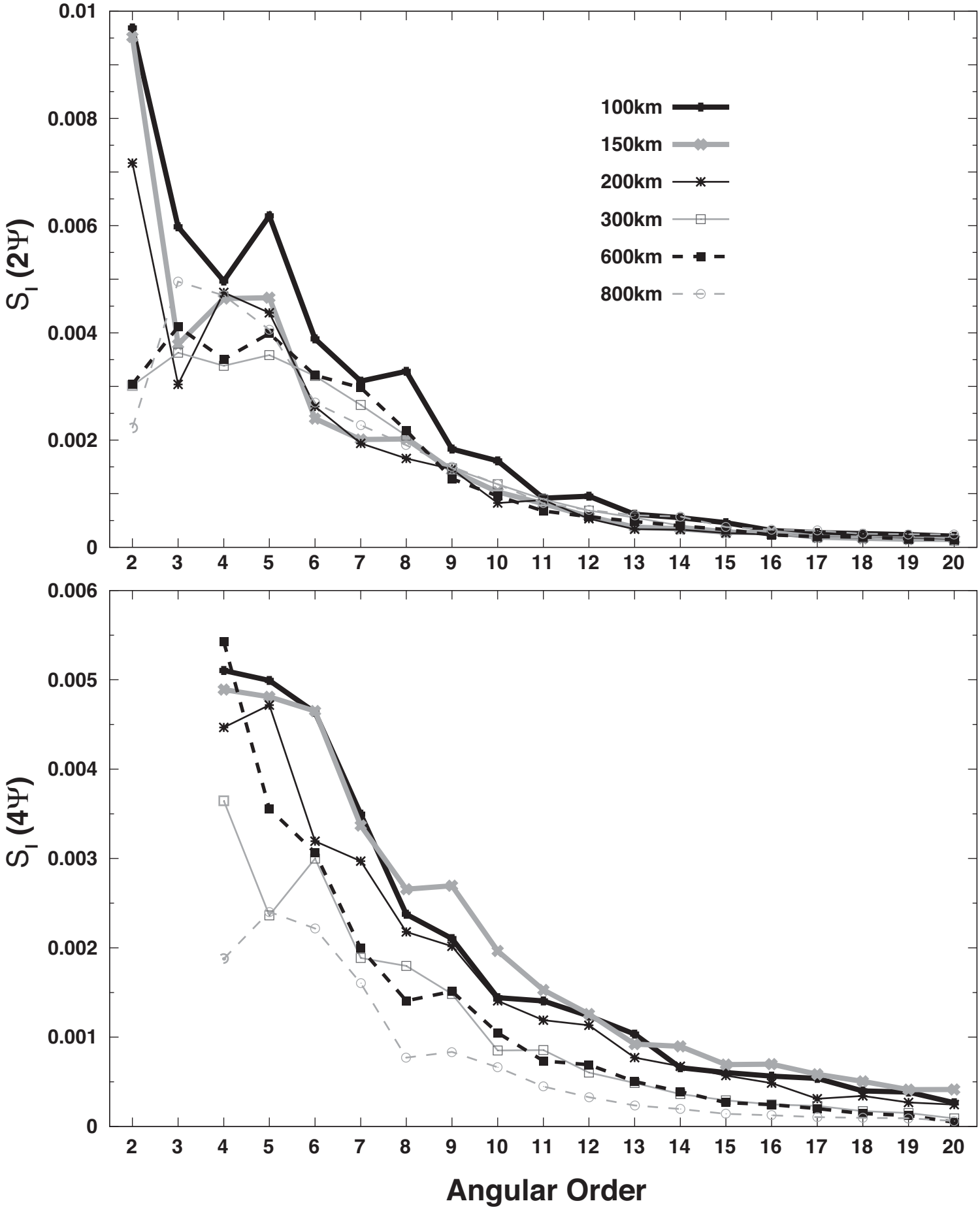
100km
150km
200km
300km
600km
800km
S_I (2Ψ)
S_I (4Ψ)
Angular Order
0.01
0.008
0.006
0.004
0.002
0
0.005
0.003
0.001
2 3 4 5 6 7 8 9 10 11 12 13 14 15 16 17 18 19 20

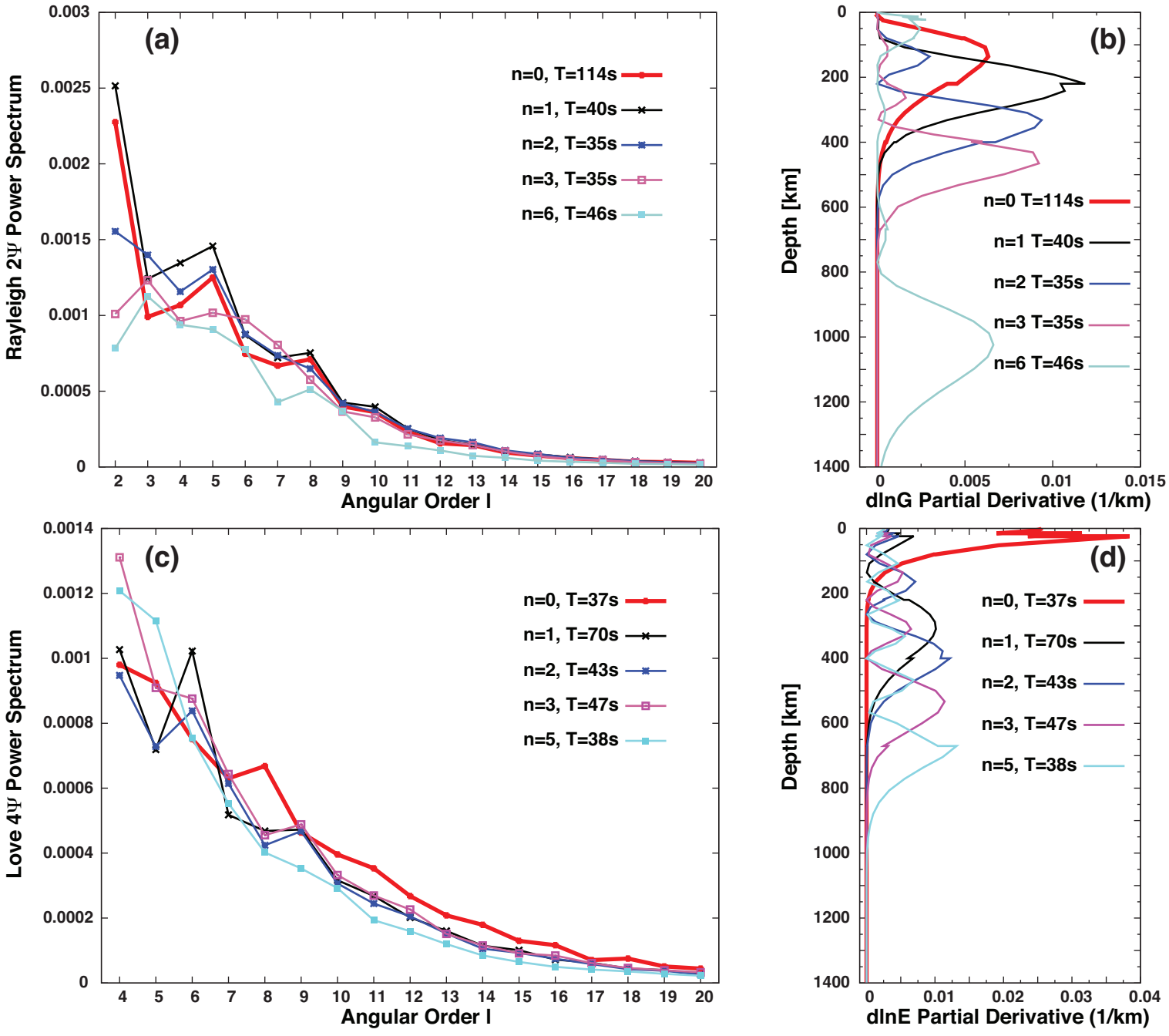
(a)
Rayleigh 2Ψ Power Spectrum
Angular Order l
n=0, T=114s
n=1, T=40s
n=2, T=35s
n=3, T=35s
n=6, T=46s
(b)
Depth [km]
dlnG Partial Derivative (1/km)
n=0 T=114s
n=1 T=40s
n=2 T=35s
n=3 T=35s
n=6 T=46s
(c)
Love 4Ψ Power Spectrum
Angular Order l
n=0, T=37s
n=1, T=70s
n=2, T=43s
n=3, T=47s
n=5, T=38s
(d)
Depth [km]
dlnE Partial Derivative (1/km)
n=0, T=37s
n=1, T=70s
n=2, T=43s
n=3, T=47s
n=5, T=38s

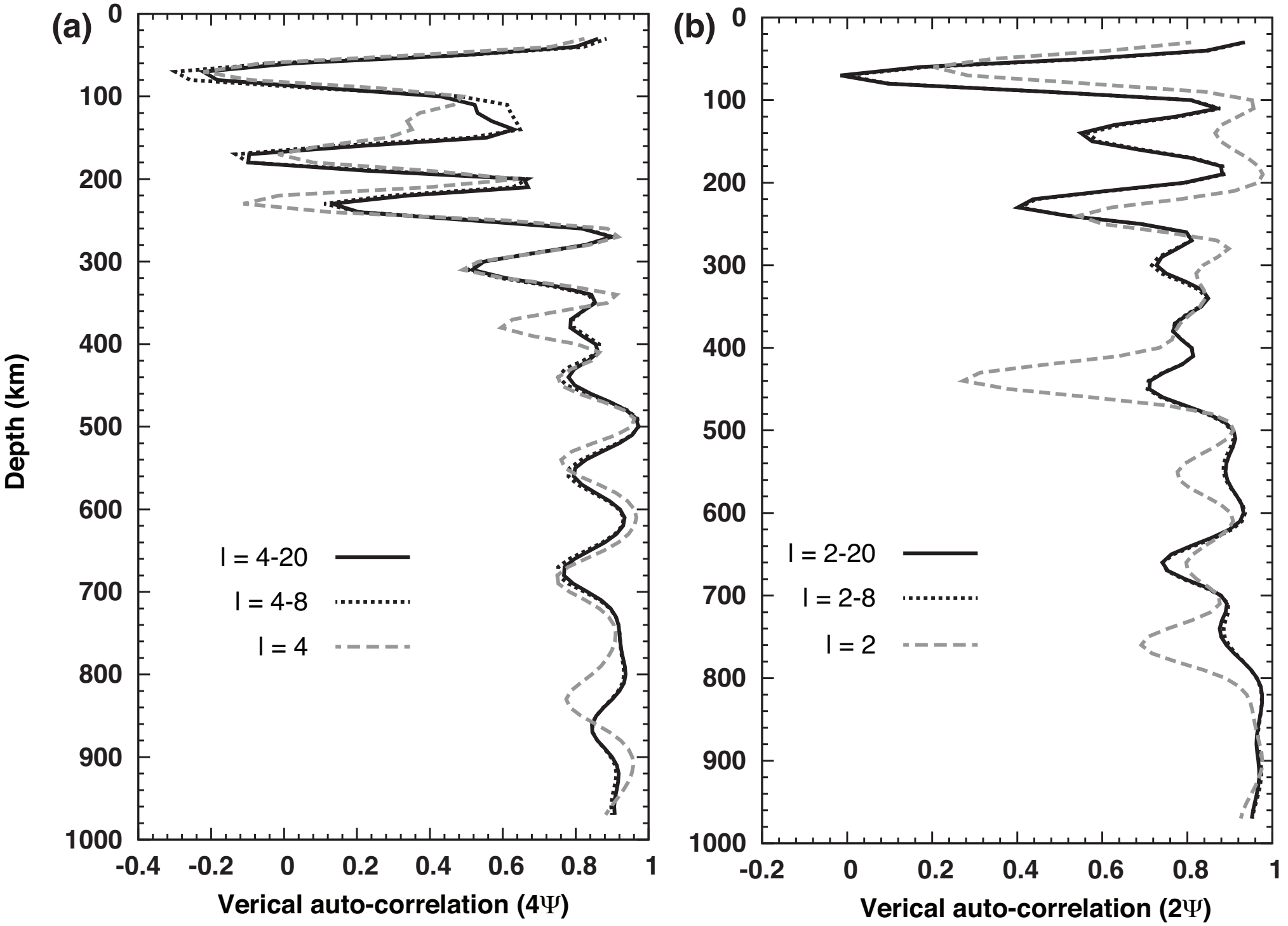
(a)
(b)
Depth (km)
0
100
200
300
400
500
600
700
800
900
1000
-0.4
-0.2
0
0.2
0.4
0.6
0.8
1
l = 4-20
l = 4-8
l = 4
l = 2-20
l = 2-8
l = 2
Verical auto-correlation (4Ψ)
Verical auto-correlation (2Ψ)